Deep Inelastic Electron - Proton Scattering at HERA Results from the H1 experiment [1]

M.W. Krasny

L.P.N.H.E
IN2P3-CNRS, Universities Paris VI et VII
4, pl. Jussieu, T33 RdC
75252 Paris Cedex 05, France
and
High Energy Physics Lab., Institute of
Nuclear Physics,Pl-30055 Cracow, Poland

H1 collaboration

Abstract: These lectures are focused on the results obtained by the H1 collaboration at HERA from the analysis of deep inelastic electron-proton scattering data collected in 1992 - the first year of HERA operation. Measurements of the structure function $F_2(x, Q^2)$, particle energy flow, jet rates and results of direct searches for leptoquarks are presented. Several experimental aspects of deep inelastic physics specific to the HERA environment are discussed.

[1] Lectures presented at the XXI International Meeting on Fundamental Physics, Miraflores de la Sierra, Madrid, May 1993

CM3/05/D

1 Introduction

The discovery of the deep inelastic electron-nucleon scattering in the late sixties at SLAC became a turning point in elementary particle physics. Protons and neutrons considered as elementary were found to be composed of point like objects called partons by Feynman. Once partons were identified with quarks - so far only mathematical objects being the fundamental representation of the SU3 symmetry of strong interactions - new trends and methods of investigations have been opened. This resulted in remarkable progress of the high energy physics over the last twenty years.

An investigation of the nucleon structure by means of deep inelastic scattering is an extension of the classical Rutheford-type experiment in which at large momentum transfer, Q, from incident lepton to a nucleon, a structure at distances of $r = h/Q$ can be revealed. In the early SLAC experiments [1, 2, 3] a scale invariant behaviour [4, 5] of the eN cross-section was observed and interpreted [6] as the incoherent scattering of electrons from freely-moving, point-like, structureless objects - quarks. The striking paradox was that quarks are apparently freely moving inside a hadron and yet free quarks had not been seen. Quantum Chromodynamics (QCD) [7] provides a natural explanation of this paradox. Being asymptotically free [8, 9] it explains why quarks are only weakly bound in the nucleon and behave as free particles in the limit of the infinite momentum transfer (at small distances). Their colour interaction becomes, however, very strong at large distances (small momentum transfers) and only colour singlets can be observed in nature. As a consequence of quark interactions, deviations from scale invariant behaviour are expected. The predictions of these deviations observed subsequently in the next generation experiments [10-17] were one of the first successes of the perturbative QCD, establishing QCD as a serious candidate for the theory of strong interactions.

These experiments were followed by several high statistics, precision experiments, which provided quantitative tests of the perturbative QCD and led to precise determination of the coupling constant of QCD [10].

The *ep* collider, HERA, in which 26.7 GeV electrons collide with 820 GeV protons, opens a new research domain in the physics of deep inelastic processes. For the first time, owing to increased centre of mass energy, processes involving partons which carry a very small fraction of the proton momentum (down to $\approx 10^{-4}$) can be studied in the perturbative ($Q^2 \geq 5\ GeV^2$) regime. Furthermore, the proton structure will be probed at 10 times smaller distances than previously accessible. The two collider experiments H1 and ZEUS, owing to their almost 4π coverage geometry, allow precise studies of hadronic systems produced in deep inelastic interactions.

In these lectures I shall discuss results obtained by the H1 collaboration from the analysis of deep inelastic scattering data collected in 1992, the first year of data taking at HERA. The data correspond to an integrated luminosity of 22.5 nb^{-1}.

2 The HERA collider

The Hera collider consists of a proton ring and an electron ring. The proton ring contains 104 sections of superconducting magnets. Each section includes: 4 dipoles, 2 quadrupoles and correction magnets. Protons accelerated by PETRA to 40 GeV are injected to the

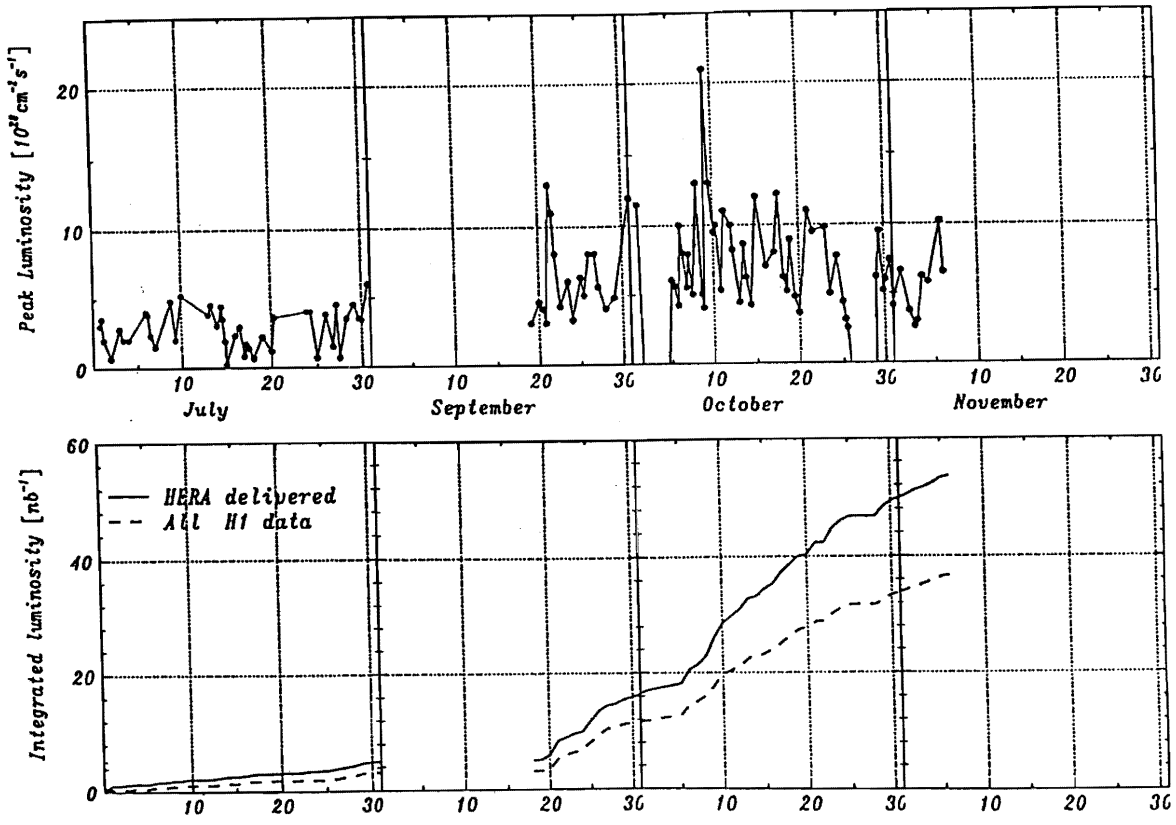

Figure 1: *Luminosity measured by the H1 luminosity system during data taking in 1992.*

HERA proton ring and accelerated to 820 GeV with warm cavities operated at the frequency of 52 MHz. The electron ring contains 416 warm magnet sections. Each section includes: 1 dipole, 1 quadrupole and 2 sextupole magnets. 12 GeV electrons injected from PETRA are accelerated to 26.7 GeV using, at present, warm cavities operating at 500 MHz frequency.

Most of the luminosity delivered by HERA in 1992 corresponds to a bunch configuration in which 10 proton bunches and 10 electron bunches are filled (the design number of circulating bunches is 210). The bunches are separated by 96 ns. Nine bunches were colliding whereas one electron and one proton bunch (called hereafter "pilot bunches") had no collision partners. Such a configuration provides the means to control the proton and electron beam induced background, as will be discussed later. The bunches were $\approx$ 60 cm (protons) and $\approx$ 1 cm (electrons) long determining the length of the collision region to be $\approx$ 30 cm (half of of the proton bunch length).

The luminosity delivered in 1992 was limited by the maximal electron current (of about 7 mA) beyond which the electron beam life time decreased rapidly. The cause of this limitation was identified at the end of the runing period to be a faulty pump, which was replaced leading to an increase of attainable long-live electron current up to $\approx$ 23 mA.

Table 1 contains a summary of the designed and 1992 HERA parameters. The evolution of the peak and the integrated luminosity over the first year of HERA operation is shown in Fig. 1.

	Design		Autumn 1992		unit
	p–ring	e–ring	p–ring	e–ring	
Energy	820	30	820	26.7	GeV
Luminosity	1.5×10^{31}		3.0×10^{29}		$cm^{-2}s^{-1}$
Integrated luminosity per year	10^5		32		nb^{-1}
Interaction points (crossing angle)	4 (0)		2 (0)		(mr)
Magnetic field	4.68	0.165	4.68	0.149	T
Number of particles	210	80	2.6	3.7	10^{11}
Current per bunch	760	290	200	280	μA
Number of bunches	210	210	10	10	
Bunch separation	96	96	96	96	ns
Injection energy	40	14	40	12	GeV
Filling time	20	15	120	30	min
σ_x/σ_y at interaction point	0.29/0.07	0.26/0.02	0.36/0.10	0.30/0.07	mm
σ_z at interaction point	110	8	≈ 200	≈ 10	mm
Energy loss per turn	6.2×10^{-6}	127			MeV
RF-frequency	52.03/208.1	499.8	52.03	499.8	MHz

Table 1: *Summary of the HERA parameters.*

3 The H1 detector

A schematic view of the H1 detector is shown in Fig. 2a. The forward-backward asymetry of the detector design reflects the difference in the electron and proton beam energies.

The detector consists of:

- The central tracking detector (1) composed of two large jet drift chamber modules, two z drift chambers and two multiwire proportional chambers. The angular coverage of the central tracker is $15^0 - 170^0$.
- The forward tracking (2), which consists of three modules of drift and multiwire proportional chambers. It covers the angular angle between 7^0 and 25^0.
- The backward multiwire proportional chamber (BPC) covering the angular region of $155^0 - 175^0$.
- A superconducting coil (6) which provides a uniform magnetic field of 1.2 T in the tracking region.
- The backward electromagnetic calorimeter (BEMC) (10), made of 88 lead - scintillator sandwich stacks, each with a depth of 22 radiation lengths, corresponding to about 1 interaction length, and with transverse dimensions of 16 by 16 cm^2.
- The LAr calorimeter, which consists of an electromagnetic section with lead absorber (3) and a hadronic section with stainless steel absorber (4). The total depth of the electromagnetic part varies between 20 and 30 radiation lengths whereas the total depth of both calorimeters varies between 4.5 and 8 interaction lengths. The LAr calorimeter covers the angular range between 4° and 153°.

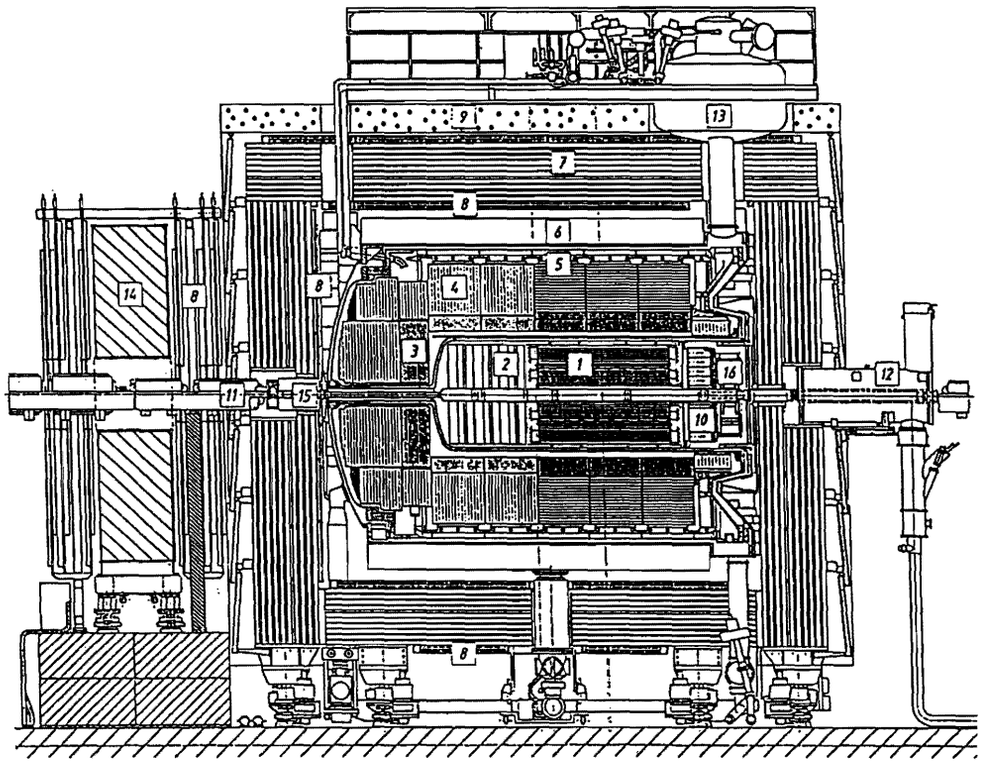

a

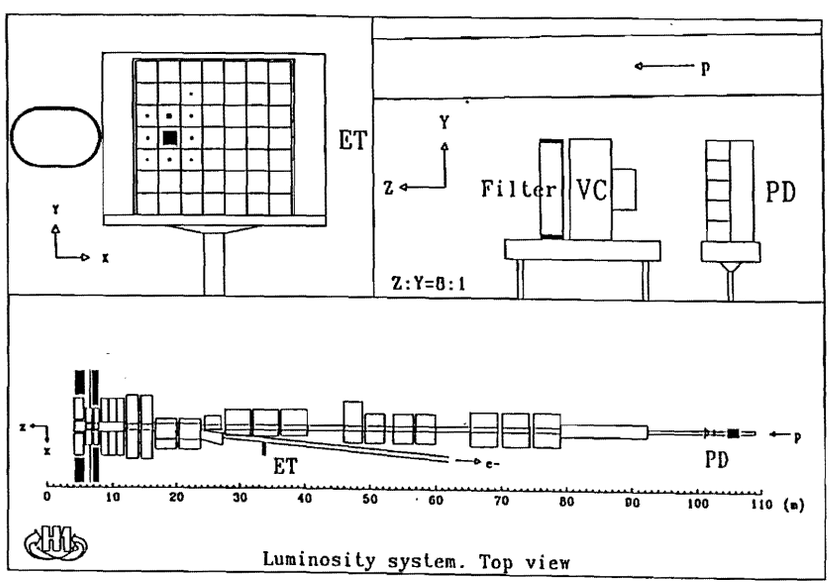

b

Figure 2: *a) Schematic view of the H1 detector. b) The layout of the H1 luminosity system.*

- The iron yoke, (7) which is instrumented with plastic limited streamer tubes and acts as muon detector and tail catcher calorimeter.

Calorimetry		
Main calorimeter: liquid Ar	Electromagnetic part	Hadronic part
Granularity	10 to 100 cm^2	50 to 2000 cm^2
Depth	20 to 30 X_0	4.7 to 7 λ_{abs}
Number of channels	30784	13568
Resolution $\sigma(E_{e,h})/E_{e,h}$	$12\%/\sqrt{E_e} \ominus 1\%$	$\approx 50\%/\sqrt{E_h} \oplus 2\%$
LAr purity - stability of el. calibration	$\leq 0.2\%$ over one year	$\leq 0.2\%$ over one month
Noise	10 to 30 MeV per channel	
Angular coverage – dead channels	$4° < \theta < 153°$	$< 0.3\%$
Backward calorimeter: Pb–scintillator		
Angular coverage – granularity	$151° < \theta < 177°$	16 x 16 cm^2
Depth – resolution $\sigma(E_e)/E_e$	22.5 X_0 (1 λ_{abs})	$10\%/\sqrt{E_e} \oplus 2$ [1]%
Tail catcher: iron–streamer tubes		
Angular coverage – granularity	$4° < \theta < 177°$	
Depth – resolution $\sigma(E_h)/E_h$	4.5 λ_{abs}	100 [50]$\%/\sqrt{E_h}$
Plug calorimeter: Cu–Si		
Angular coverage – granularity	$0.7° < \theta < 3.3°$	5 x 5 cm^2
Depth – resolution $\sigma(E_h)/E_h$	4.25 λ (44.6 X_0)	$\approx 150\%/\sqrt{E_h}$
Electron tagger: Tl(Cl/Br)		
Angular coverage – granularity	$\theta > 179.7°$	2.2 x 2.2 cm^2
Depth – resolution $\sigma(E_e)/E_e$	21 X_0	$\approx 10\%/\sqrt{E_e} \oplus 1\%$
Tracking		
Coil: radius – field	3 m – $B = 1.15$ T, $\Delta B/B \leq 2\%$	
Central tracking		
Angular – radial coverage	$25° < \theta < 155°$	$150 < r < 850$ mm
Jet chamber: spatial resolution	$\sigma_{r\phi} = 170\,\mu m$	$\sigma_z = 22.0$ mm
z-chambers: spatial resolution	$\sigma_{r\phi} = 25$ and 58 mm	$\sigma_z \approx 350\,\mu m$
Momentum – dE/dx resolution	$\sigma_p/p^2 < 1.0$ [0.003] GeV^{-1}	$\sigma(dE)/dE = 10$ [6]%
Forward tracking		
Angular – radial coverage	$7° < \theta < 25°$	$120 < r < 800$ mm
Spatial resolution	$\sigma_{r\phi} = 170\,\mu m$ ($\sigma_r = 29$ mm)	$\sigma_{x,y} = 210\,\mu m$
Trigger proportional chambers		
Angular coverage – channels	$7° < \theta < 155°$	4000
Muon detection		
Instrumented iron		
Angular coverage – total area	$4° < \theta < 171°$	4000 m^2
Number of channels	wires: 103700, strips: 28700, pads: 4000	
Spatial resolution	$\sigma_{wire} = 3 - 4$ mm	$\sigma_{strip} = 10 - 15$ mm
Angular – momentum resolution barrel	$\sigma_\theta(\sigma_\phi) = 15(10)$ mr	$[\sigma_p/p \approx 0.35]$
Forward muon toroid		
Angular coverage – resolution	$3° < \theta < 17°$	$[0.25 < \sigma_p/p < 0.32]$
Overall size (x, y, z) – weight	12 x 15 x 10 m^3	2800 t

Table 2: *Summary of the H1 detector parameters.*

- Muon detection system consisting of muon chambers added inside and outside of the iron yoke (8) and a forward spectrometer consisting of an iron toroid (14) and 6 layers of drift chambers (8).

- The time of flight (TOF) system (16), located behind the backward calorimeter, which consists of two scintillator planes, each with a time resolution of about 3 ns, and provides a separation of genuine *ep* events from proton beam-wall and beam-gas

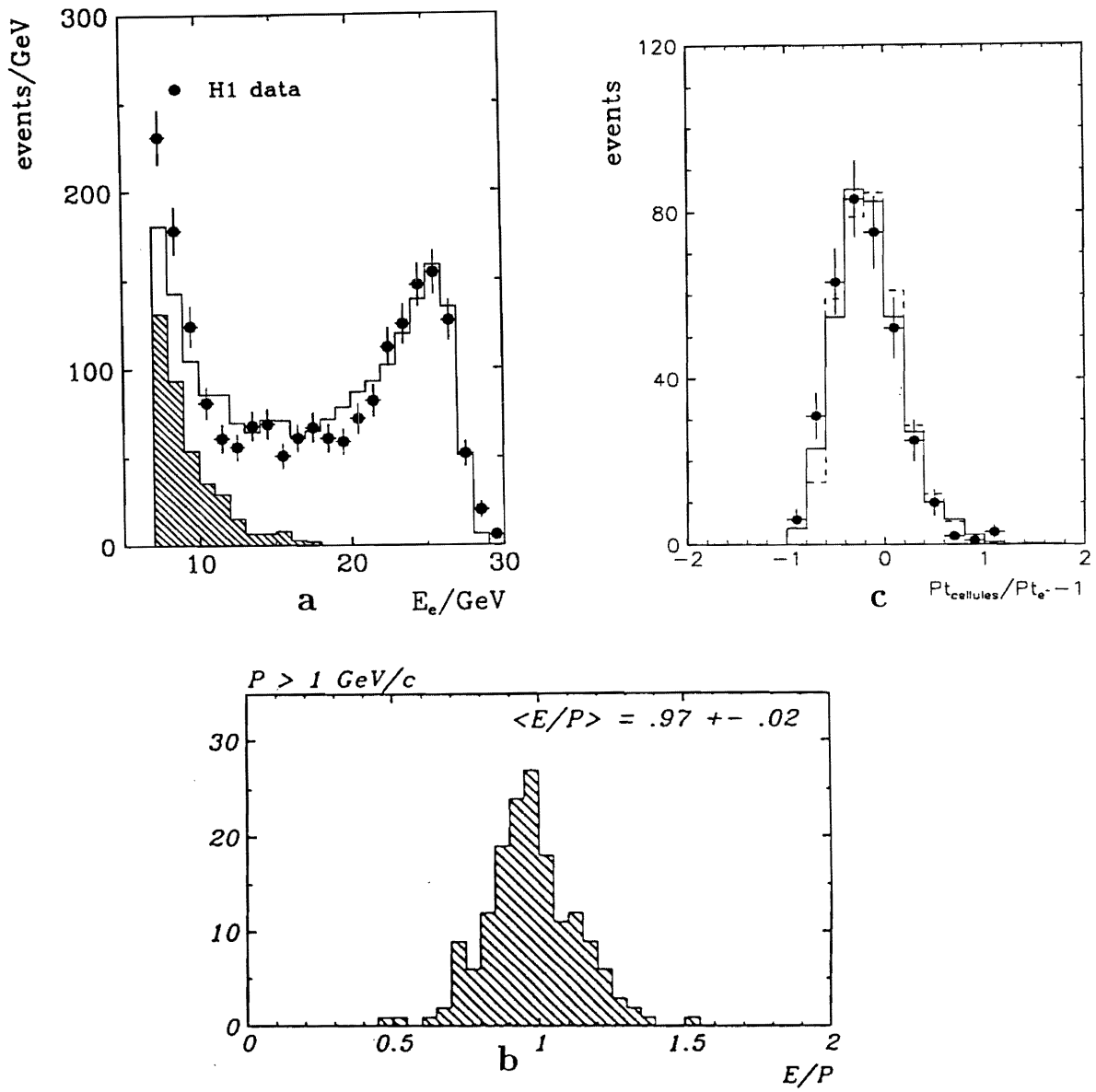

Figure 3: *a) Distribution of the scattered electron energy in the BEMC. The solid histogram is the Monte-Carlo predictions. The shaded histogram is the the predicted background due to γp scattering. b) Ratio of the electron energy as measured in the LAr calorimeter and the elctron momentum as measured in the CJC. c) Ratio of transverse momentum of the scattered electron and of the hadronic system (BEMC/LAr cross-check). The lines represent Monte-Carlo simulations using two different hadronization models.*

interactions upstream of the detector at the first trigger level.

- The luminosity detector system shown in Fig. 2b which provides detection of the the $e-\gamma$ coincidence from the reaction $e+p \rightarrow e+\gamma+p$. The electron tagging calorimeter is located at the distance of 33m from the interaction region in the backward or $-z$ direction and detects electrons scattered at small angles (less than 5 mrad with respect to the electron beam direction). The photon tagging calorimeter is located at $z = -103$m and detects photons at angles less than 0.5 mrad with respect to the electron beam direction (both detectors are TlCl/TlBr crystal calorimeters).

A summary of the H1 detector parameters is given in table 2.

The most important information for the analysis of the deep inelastic scattering at HERA is provided by the calorimeters which measure the energies of the scattered electrons and produced hadrons. Their performance was studied using both the deep inelastic and the cosmic muon data leading to the determination of the absolute scale of the calorimeters (the relative calibration of various calorimeter sections has been obtained using beam test measurements).

The absolute energy scale of the BEMC was determined using deep inelastic scattering events exploiting the redundancy in the measurement of the deep inelastic scattering kinematics. The measured electron energy in the BEMC was compared with the one determined from the angle of the hadronic system and the electron angle leading to the determination of the energy scale with a precision of 3 % [11]. Fig. 3a shows the distribution of the scattered electron energy for selected sample of deep inelastic events compared with a Monte Carlo simulation after adjusting the BEMC energy scale. A very good agreement is observed in the region where deep inelastic processes dominate, i.e. in the region of a large deposited energy.

The absolute scale of the energy response of the LAr calorimeter at HERA was verified by comparing the momenta of charged particles, measured in the central tracker, with associated energy deposited in the calorimeter. Using electron and positron tracks produced by cosmic ray muons, the electromagnetic scale has been checked to $\pm 3\%$ [12] as shown in Fig. 3b. In addition, a study was carried out of the balance of transverse momentum between the scattered electron measured in the BEMC and the recoiling hadronic system measured in the LAr calorimeter, leading to the determination of present uncertainty of the overall hadronic energy scale of the LAr calorimeter of $\pm 7\%$ (see Fig. 3c).

4 Deep inelastic electron proton scattering

4.1 Reconstruction of the kinematical variables

The process discussed throughout these lectures is shown schematically in Fig. 4. Here $k = (E_o, \overline{k})$ and $k' = (E_e, \overline{k}')$ are 4-momenta of the incident and scattered electron and P is the 4-momentum of the proton.

In the low Q^2 region the exchanged particle is a virtual photon. The diagram shown in Fig. 4 is the lowest-order diagram corresponding to the Born approximation. The higher-order diagrams yield corrections to the cross-section which will be referred to as radiative corrections.

It is convenient to introduce the following variables:

$$\begin{aligned} Q^2 &= -(k' - k)^2 = -q^2 \\ W^2 &= (P + q)^2 \\ x &= \frac{Q^2}{2Pq} \\ y &= \frac{Pq}{Pk} \end{aligned} \tag{1}$$

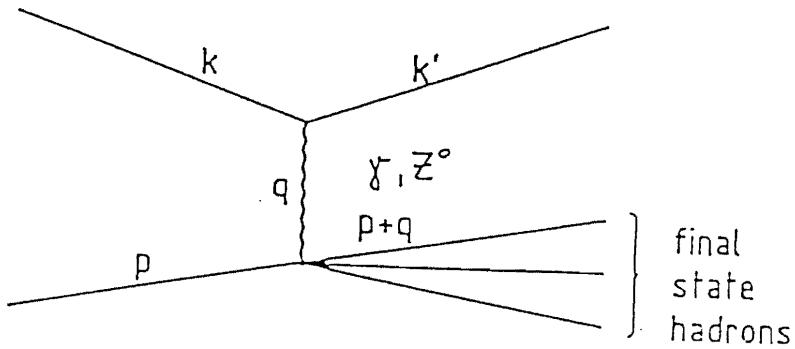

Figure 4: *The Born diagram for electron - proton scattering.*

The H1 experiment at HERA measures both the scattered electron and the hadronic final state, providing various methods of determining the kinematical variables defined above. This novel feature of the H1 experiment, compared to the fixed target ones, provides an important cross-check of systematic effects. In particular, the cross-section determined in terms of various variable sets has a different sensitivity to the processes of real photon emission from the incoming and scattered electron leading to an experimental cross-check of radiative corrections.

At the fixed centre-of-mass energy and in the absence of radiative processes involving real photons only two out of these variables are independent. Let us choose x and Q^2 as variables describing the scattering process. Their dependence on the energy of the scattered electron and its angle is illustrated in Fig. 5a whereas in Fig. 5b lines of constant energy of the recoil quark jet and its angle are shown.

In the analysis of the data recorded in 1992 two distinct reconstruction methods were used by the H1 collaboration. In the first method y is reconstructed from the energy E_e, the polar angle θ_e, of the scattered electron measured relative to the proton beam direction, and from the known energy of the incident electron, E_o

$$y_e = 1 - (E_e/E_o)\sin^2(\theta_e/2). \tag{2}$$

In the second reconstruction method y is determined from the hadrons using the relation [13]

$$y_h = \sum_{hadrons} \frac{E_h - p_{z,h}}{2E_o}, \tag{3}$$

where E_h is the energy of a hadron and $p_{z,h}$ its momentum component along the incident proton direction. The 4-momentum transfer Q^2 is determined from the electron observables θ_e and E_e as

$$Q_e^2 = 4E_oE_e\cos^2(\theta_e/2), \tag{4}$$

and x is calculated using the electron variables

$$x_e = Q_e^2/(sy_e), \tag{5}$$

or, by combining the hadron measurement of y and the electron measurement of Q^2

$$x_m = Q_e^2/(sy_h). \tag{6}$$

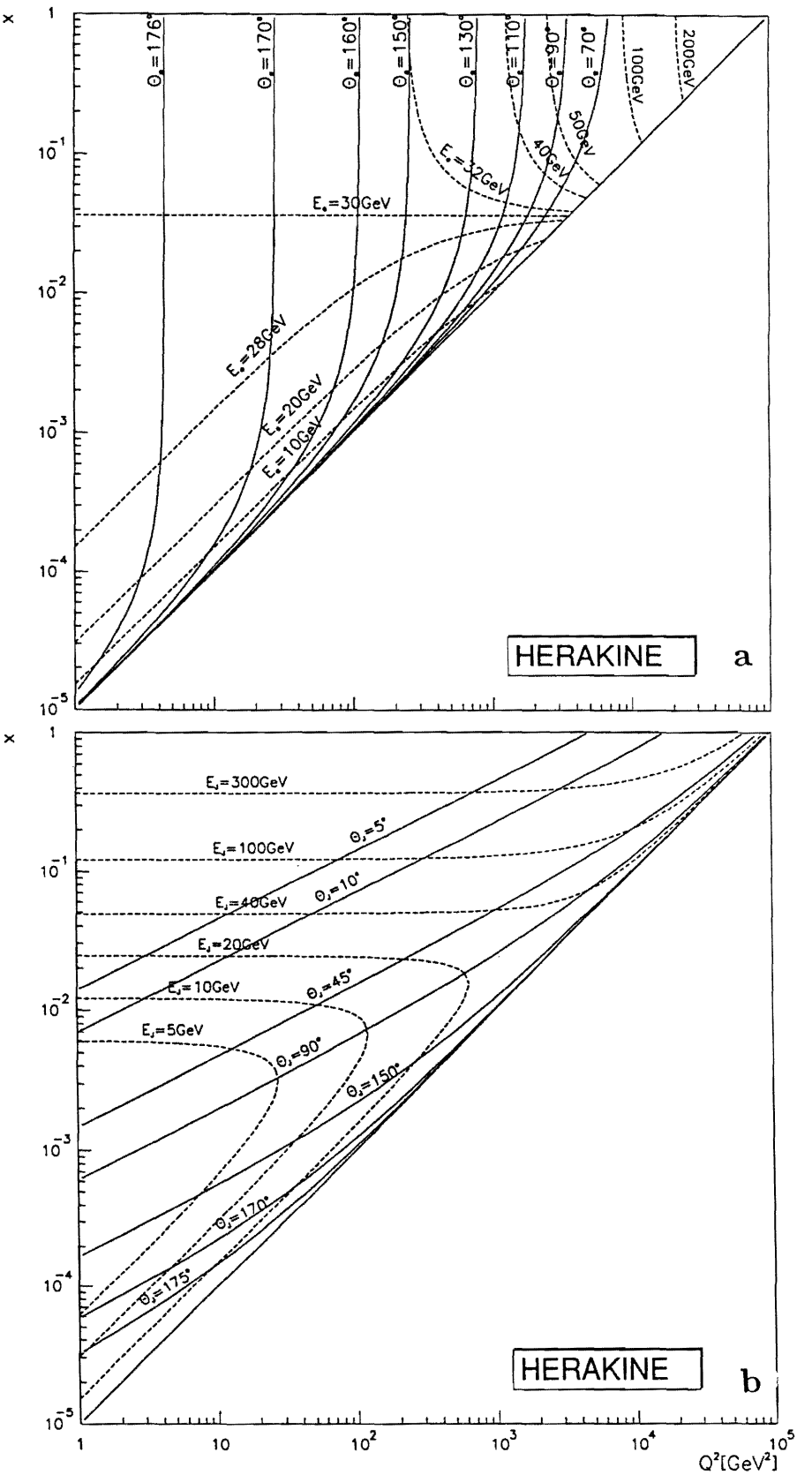

Figure 5: *a) Lines of constant scattered electron energy and angle. b) Lines of constant current-quark energy and angle. ($E_o = 30GeV$, courtesy of Jean-François Laporte)*

The centre-of-mass energy squared, s, is given by

$$s = 4E_oE_p, \tag{7}$$

where E_p is the incident proton energy.

The energy of the scattered electron E_e is measured in the electromagnetic calorimeters: in the BEMC at low Q^2 (below about 100 GeV^2) and in the LAr at higher Q^2. The polar angle θ_e of a low Q^2 scattered electron was calculated from the position of the reconstructed event vertex and a reconstructed space point in the backward proportional chamber (BPC). The vertex position is determined on an event by event basis, from at least one track reconstructed in the CJC, originating from the interaction region. At higher Q^2, θ_e is calculated from the position of the centre of gravity of the reconstructed electron cluster and from the position of the reconstructed vertex. The hadron energies and angles are measured in the LAr, the BEMC and the instrumented iron backing calorimeter as well as redundantly from charged particle tracks measured in the central drift chamber.

In the determination of y_h, according to relation 3, combined calorimetric measurements and reconstructed charged tracks in the central region are used. The contribution of tracks to the y_h measurement is about 40 % which reduces the influence of energy scale uncertainties.

4.2 Physics aspects of deep inelastic scattering at HERA

The physics aspects of deep inelastic scattering at HERA were discussed extensivelly at this school by A. Martin and W. Buchmuller. Bellow some of the aspects are briefly recalled.

HERA, owing to its large centre-of-mass energy, provides means to extend studies of the proton structure towards smaller distances than achieved in the fixed target experiments. In addition, for the first time, processes involving "wee partons", i.e., partons carrying a fraction of the proton momentum down to $\approx 10^{-4}$ can be investigated and confronted with the perturbative QCD.

The Q^2 evolution of parton densities measured in the fixed target experiments is well described by the perturbative QCD [10], using the Gribov-Lipatov-Altarelli-Parisi (GLAP) equations [14]. The GLAP equations were derived for the large Q^2, large x region, where terms $\sim \alpha_s \lg Q^2$ are dominant. These equations neglect terms of the order of $\sim \alpha_s \lg(1/x)$, which become dominant in the low x region. Here, the adequate evolution equation, which sums up all $\sim \alpha_s \lg(1/x)$ terms, is that of Balitski, Fadin, Kuraev and Lipatov (BFKL) [15]. This evolution equation predicts a fast rise of parton densities in the low x region. In the large parton density system, processes of parton-parton rescattering, leading eventually to a saturation of parton densities, can be observed and analysed using the perturbative QCD. Therefore, measurements in the low x region at HERA will provide novel means of confronting predictions of the perturbative QCD with the data.

The above discussion is illustrated in Fig. 6, where the regions of validity of GLAP and BFKL equations are shown together with a "critical line" defining a region where parton rescattering processes become important [16]. Note that the scale of the $\lg(1/x)$ on this plot is not fixed by QCD and it remains to be demonstrated experimentally if HERA will access the BFKL domain.

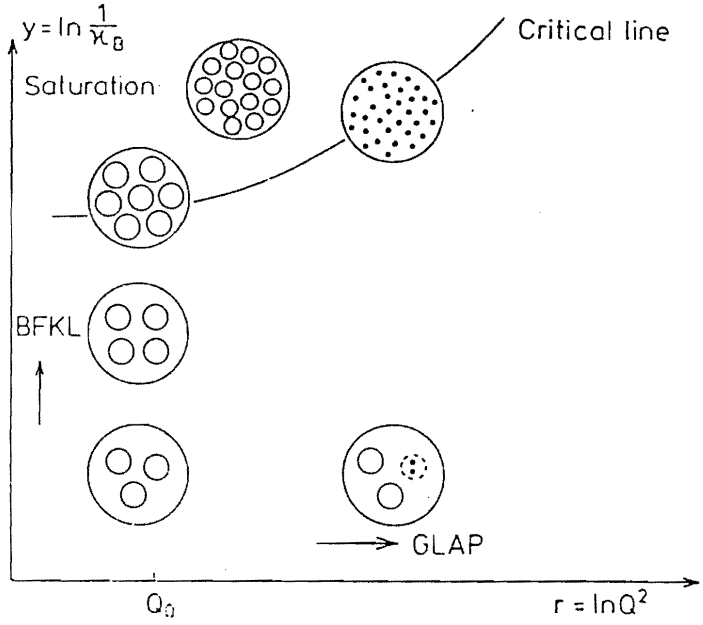

Figure 6: *Regions of validity of the BKFL and of the GLAP evolution equations.*

Several measurements can be made at HERA to establish novel effects in the low x region including: measurements of structure functions, measurements of jets associated with deep inelastic scattering at low x, particle correlations, etc. At present only measurement of the structure function F_2 can yield statistically significant results, as will be discussed in section 6.

At HERA the perturbative QCD can be tested in processes of jet production associated with deep inelastic scattering at large Q^2. In contrast to the LEP experiments, where large jet statistics have been accumulated at the fixed virtuality scale, at HERA evolution of jet rates as a function of Q^2 can be observed in a single experiment. This will enable in the future a precise determination of the running coupling constant α_s. The H1 results on jet production are discussed in section 7.

The HERA collider can be considered as a dedicated machine to look for leptoquarks and leptogluons in the region of their masses and couplings where no constraints from other experiments can be expected. Leptoquarks and leptogluons appear naturally in various extentions of the standard model. The searches for these particles in the H1 1992 data will be discussed in section 8.

5 Experimental aspects of deep inelastic scattering at HERA

5.1 Introduction

A review of fixed target deep inelastic scattering experiments and their results has been presented by R. Voss at this school. In this section I shall concentrate only on some experimental aspects which represent novel challenges for deep inelastic experiments operating

in the colliding mode at higher energy than previously attainable. Those are: luminosity measurement, selection of the deep inelastic scattering events in the collider environment, means to control the photoproduction background and experimental control of radiative corrections.

5.2 Luminosity measurement

For the absolute luminosity measurement, detection of well calculable ep processes is required. These processes must involve small momentum transfer to protons ($Q^2 \ll M_P^2$), so that the uncertainty related to an internal proton structure can be avoided. This constraint makes the luminosity measurement at HERA less precise ($\approx$ 7% accuracy) than in the fixed target experiments using charged leptons (neutrinos), where the accuracy achieved was $\approx$ 2%(5%).

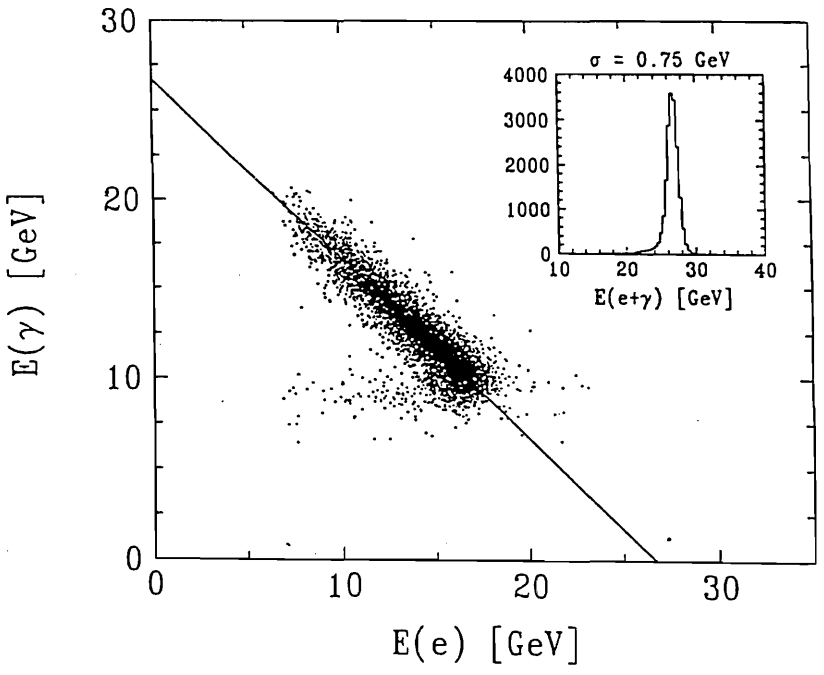

Figure 7: $e - \gamma$ *energy correlation for the elastic radiative scattering events detected by the H1 luminosity calorimeters.*

This is mostly due to the difficulty of measuring low Q^2 processes in the beam colliding mode, where effects of beam dynamics are interplaying with the experimental signatures of the measured process.

For the data accumulated in 1992 the process of the elastic radiative scattering $ep \rightarrow ep + \gamma$ was used. This process gives rise to a high counting rate and may serve for luminosity monitoring even at very low beam intensity. Both e and γ emerge from this process at very small angles ($\theta \leq 0.5$ $mrad$ with respect to the electron beam) and are detected in the luminosity calorimeters described in section 3. The experimental signature of elastic radiative scattering is a coincidence of signals in the γ - tagger and e - tagger such that the sum of deposited energies correspond to the energy of the electron beam. In Fig. 7 correlation between the measured electron and γ energies are shown exhibiting

a clear signal of the elastic radiative scattering events. The luminosity is determined from the rate of these events. The background is determined from the rate of observed events associated with the electron pilot bunch, where all coincidences are due to electron-gas and electron-collimator interactions. The largest uncertainty is orginating from the precision of monitoring the electron beam tilt in the vertical and horizontal planes. The achieved precision of 0.02 *mrad*, corresponds to an error of $\leq 7\%$ of the measured luminosity. All results discussed in these lectures will be subject to this overall normalization uncertainty.

5.3 Selection of deep inelastic scattering candidates

In Fig. 8a and 8b displays of deep inelastic neutral current events observed in the H1 detector are shown. In the event shown in Fig. 8a the scattered electron give rise to an electromagnetic energy deposit in the BEMC, whereas associated current-quark and proton-remnant jets are observed both in the central jet chamber and in the LAr calorimeter (this class of events will be called hereafter the "low Q^2" class). In the event shown in Fig. 8b the scattered electron is observed in the LAr calorimeter and is balanced by a high energetic quark current jet observed back-to-back in the LAr calorimeter and in the tracker (this class of events will be called hereafter the "high Q^2" class).

Events of these types represent a tiny fraction (about 10^{-4}) of all events in which sizeable energy is deposited in the H1 detector. Their efficient triggering and fast data reduction is a real challenge at HERA. In the H1 detector the deep inelastic candidates are triggered by requiring a localised energy deposit of more than 4 *GeV* in the BEMC or by requiring a significant transverse energy observed in the LAr calorimeter. The low Q^2 BEMC trigger is dominated by interactions of beam protons with residual gas and beam line elements upstream of the H1 detector. The majority of these events are efficiently rejected early, at the trigger level, using a time of flight system (TOF) installed behind the BEMC. A reduction of the rates owing to the TOF system is illustrated in Fig. 9. The reduction factor provided by TOF was sufficient at the instantenous luminosity delivered by the accelerator in the 1992 to make further selections in the off-line analysis. The "low Q^2" deep inelastic scattering candidates were selected off-line by the following requirements:

- A BEMC energy cluster was required to be associated with at least one reconstructed space point in the BPC. The distance between the cluster centre-of-gravity and the BPC space point was required to be smaller than about 3 σ of the cluster position resolution.
- The lateral size of the cluster was required to be smaller than 5 *cm*, as expected from beam test results for the signature of an electron.
- The number of tracks pointing outside the interaction region had to be small.
- An event vertex, reconstructed from tracks in the central tracker, within ± 50 *cm* from the nominal interaction point was required in order to determine the electron scattering angle.
- The missing energy, defined as $E_{miss} = E_o \cdot (y_e - y_h)$, was required to be smaller than 11.7 *GeV*.

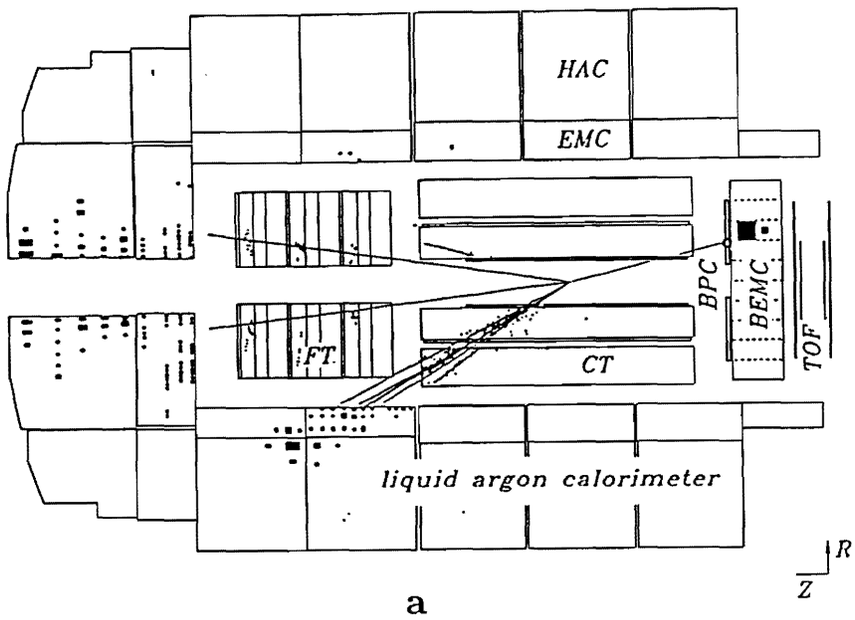

a

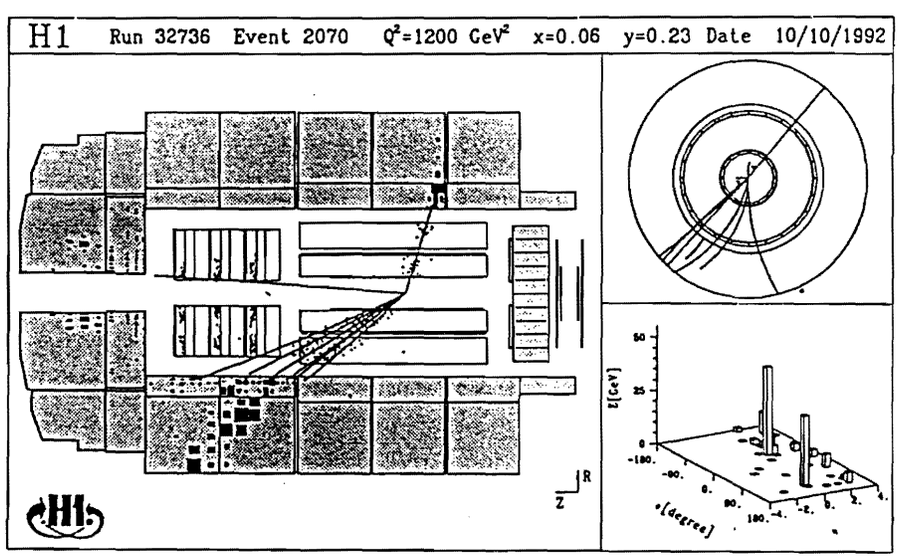

b

Figure 8: *Deep inelastic scattering events in the H1 detector: a) an event belonging to the "low Q^2" sample b) an event belonging to the "high Q^2" sample*

In addition to the above criteria the following kinematical criteria had to be fulfiled for the "low Q^2" sample:

- An electron candidate was demanded to be reconstructed with an angle $160° < \theta_e < 172.5°$ with respect to the proton beam axis to ensure full containment of the electron shower in the BEMC calorimeter

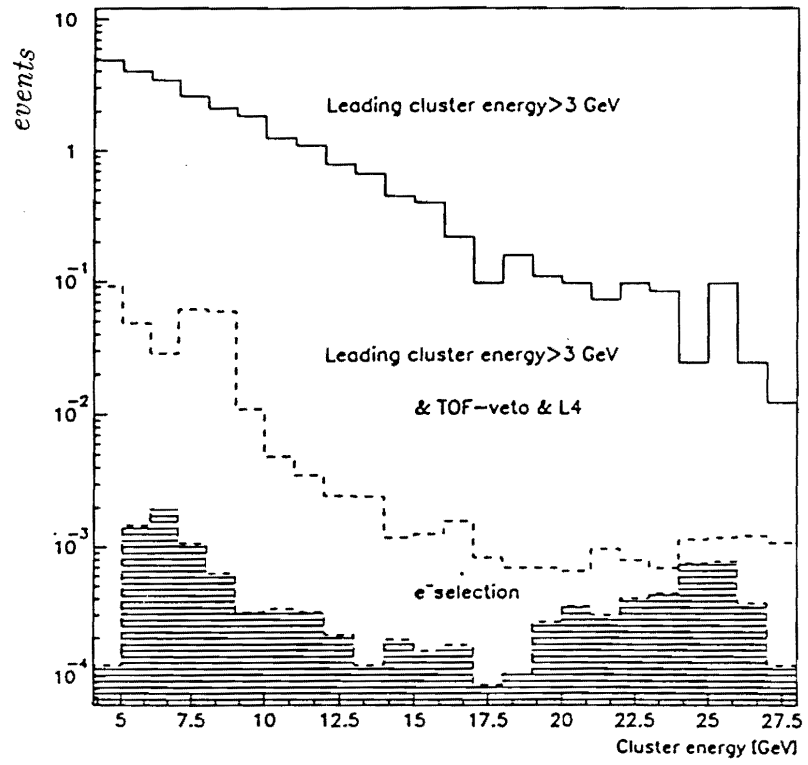

Figure 9: *Reduction of event rate ("low Q^2" sample) at various stages of event filtering as a function of the cluster energy in the BEMC.*

- The energy of the scattered electron, E_e, had to be larger than $E_e > 10.4$ GeV for the analysis of the structure functions $E_e > 14.0$ GeV for the analysis of the hadronic final states to avoid, in the later case, a photoproduction contribution, which in the analysis of structure functions was statistically subtracted.

The "high Q^2 sample" consists of events with the scattered electron detected in the LAr calorimeter. This sample was selected off-line by the following requirements:

- The electromagnetic cluster in the LAr calorimeter having the largest transverse energy (the scattered electron cluster) was fully contained in the LAr calorimeter.
- There was no muon track candidate within a cone of half opening angle of 5° around an electron cluster (to reject cosmic showers),
- The energy deposited in the electromagnetic section in a cylinder of radius between 15 and 30 cm around the electron direction had to be less than 1.2 GeV.
- The energy deposited in the hadronic section within 30 cm around the electron direction had to be less than 0.5 GeV
- As with the "low Q^2" sample, at least one charged particle track was required in the central tracking system to define an event vertex within ±50 cm from the nominal interaction point.
- $Q^2 > 100$ GeV^2 and $y < 0.7$,

In addition, for the analysis of the hadronic final states an explicit cut on the invariant mass W, $W^2 > 5000$ GeV^2, was made to ensure large enough hadronic energy flow into the detector.

It is worthwhile to point out that the deep inelastically scattered electron is identified and measured uniquelly by calorimetric means and, in particular, no requirement of the presence of a negative track (present in most of the fixed target DIS experiments) is made. This leads, on one hand, to higher uncertainty of the photoproduction contamination in the large y, low E_e region (this contribution was controlled by identifying the charge of the scattered lepton candidates in the magnetic spectrometers), but, on the other hand, to significantly smaller radiative corrections for real photon emission processes from the outgoing electron (as will be discussed later).

Another important aspect of selecting deep inelastic scattering candidates in the H1 detector at HERA is that the interaction vertex is required to be reconstructed, on an event-by-event basis, using secondary hadrons. This requirement leads to losses of events

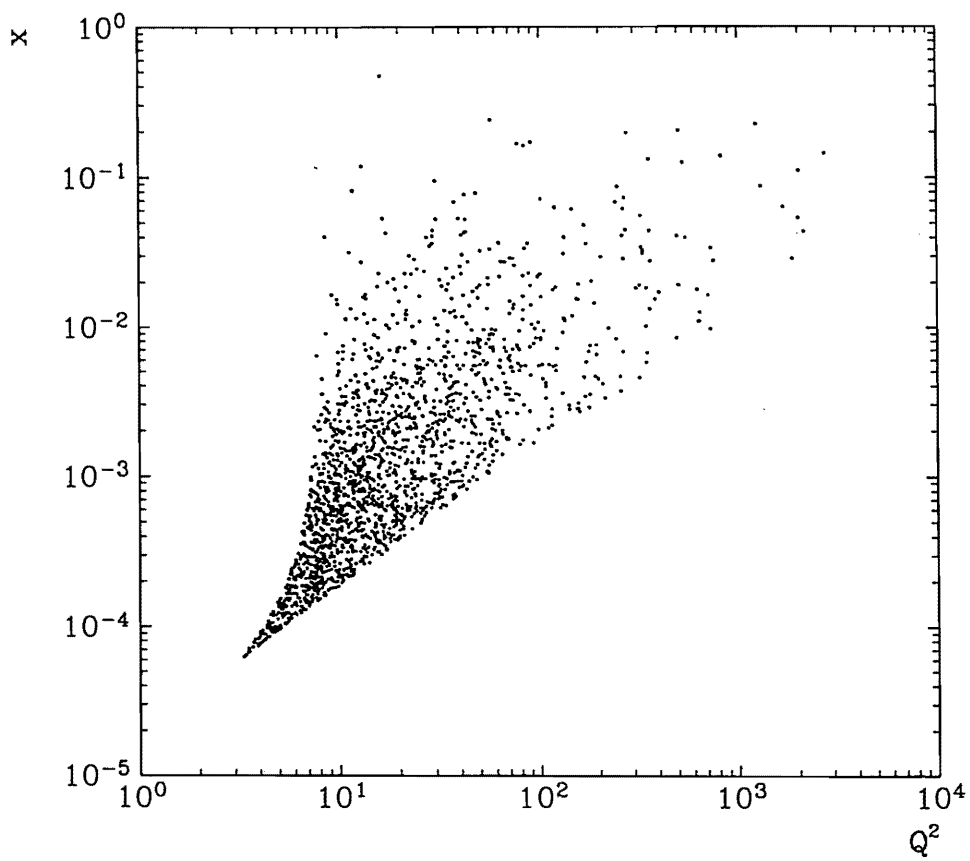

Figure 10: *Distribution of the selected deep inelastic scattering events on the x, Q^2 plane.*

in the high x region, where hadrons are emitted at small angles and do not leave reconstructed tracks in the detector (they are lost in the beam pipe).

The geometry of the H1 experiment and the size of the beam pipe impose a severe constraint on the maximal angle (lowest Q^2), above which the electron is not measured.

All these limitations are visible in Fig. 10, where the distribution of deep inelastic candidates on the (x, Q^2) plane is shown. Losses of high x events as well as the sharp angular cut-off (left side of the plot) are visible.

At HERA the size of the beam related background can be studied directly, owing to the bunch structure described in section 2. Any event passing cuts specified in this section but orginating from the pilot bunch interactions would indicate the presence of the beam related background. In the event sample of deep inelastic candidates no single pilot bunch event passed the selection criteria.

5.4 Photoproduction background subtraction

As was mentioned in the previous section the most important limitation in extending the measurement domain towards high y (small x) comes from the background of photoproduction processes.

These are ep collisions at $Q_e^2 \rightarrow 0$, which outnumber by several orders of magnitude the deep inelastic collision rate. In these collisions the electron is scattered at small angle and is not observed in the BEMC. However, the hadrons produced in the collision may give rise to a signal in the BEMC, which could be missidentified as that of a deep inelastically scattered electron.

The contribution of these events to the deep inelastic event sample is controlled at HERA by selecting deep inelastic candidates which have a detected electron in the electron tagger and therefore constitute a clean $\gamma - p$ background event sample in which a fake electron has been found in the main detector. The energy spectrum and the angular distribution of fake electron candidates is shown in Fig. 11a and 11b respectively, and compared with the Monte-Carlo simulation containing both soft and hard $\gamma - p$ processes in a proportion found in the analysis ot the $\gamma - p$ interactions [17]. The photoproduction background events are concentrated in the region of small energies and large angles. The Monte-Carlo simulation describes well both the energy spectrum and the angular distribution of the fake electrons from the "tagged sample". This Monte-Carlo model can thus be used to calculate the residual photoproduction background corresponding to the full data sample (tagged and untagged). At low energies the background becomes higher than the signal and one can no longer rely on the Monte-Carlo predictions. This leads to an energy cut $E_e = 10.4GeV$ discussed in the previous section.

A significant fraction of the remaining photoproduction background events was rejected by imposing the missing energy cut defined in the previous section. For $\gamma - p$ events, the scattered electron is missing, leading to a large value of E_{miss}. This cut rejects, as well, radiative deep inelastic scattering events in which a hard photon is emitted in the direction of the incoming electron. The above cut is very effective owing to almost complete angular coverage of the hadronic calorimeter and provides a novel tool (with respect to the fixed target DIS experiment) for reducing both the size of the photoproduction background and the size of radiative corrections (as will be discussed in the next section).

The residual photoproduction background was subtracted statistically. In the sample of events selected for the structure function determination this background was found to be less than 30 % at the $y \approx 0.6$ (lowest energy E'_e), becoming negligible at $y \leq 0.4$.

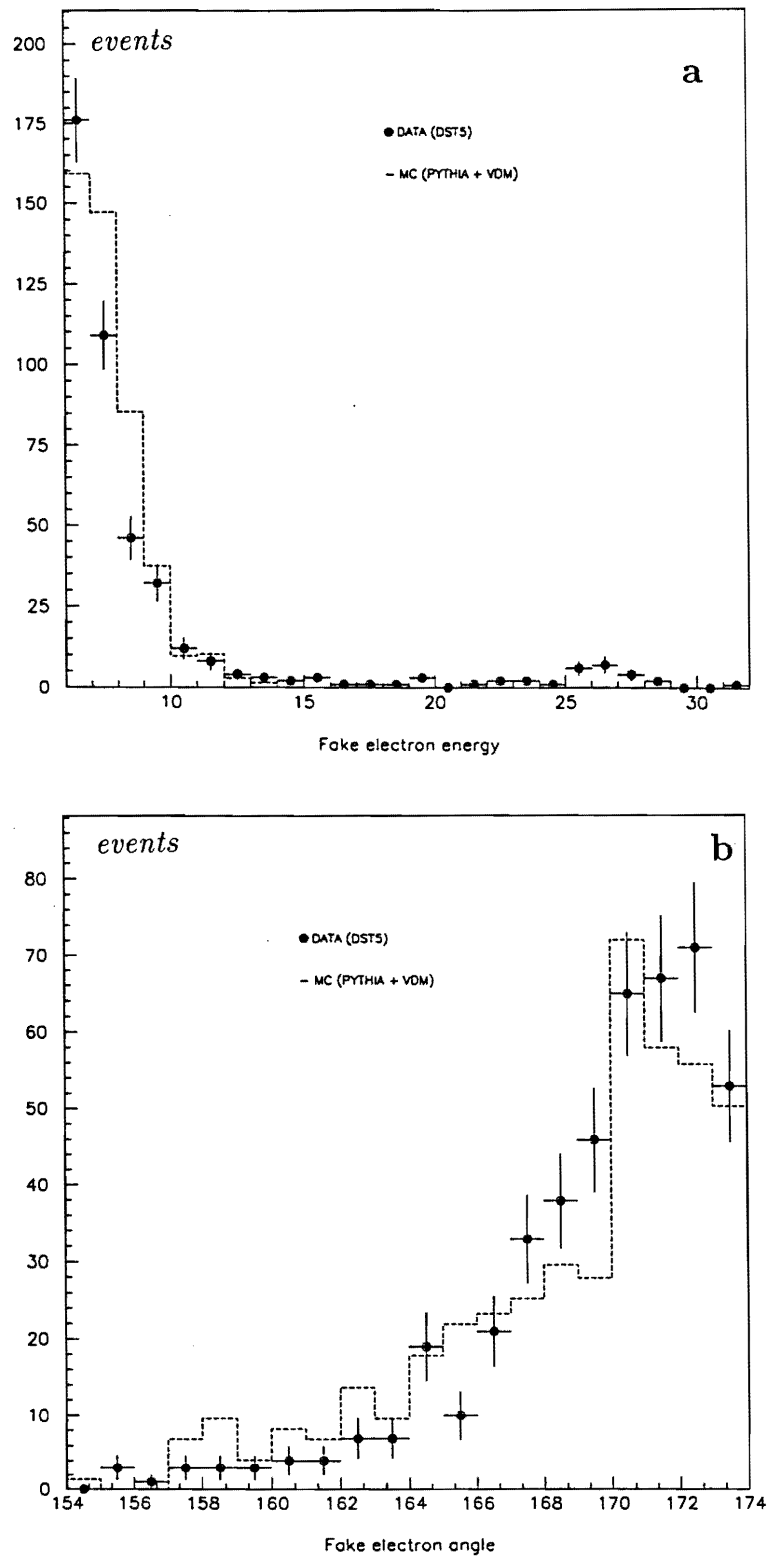

Figure 11: *Distribution of the fake electron energy (a), fake electron angle (b) for events in which electrons are observed in the electron tagger. The lines represent the Monte-Carlo predictions (see text).*

5.5 Radiative corrections

The cross-section for radiative scattering :

$$ep \rightarrow e + \gamma + X$$

is large [18] and, especially at small x, can be of the same order of magnitude as the non-radiative cross-section. In the majority of previous deep inelastic experiments, the above process could not be distinguished from the non-radiative scattering:

$$ep \rightarrow e + X$$

As a consequence, the corresponding radiative corrections had to be calculated and applied to the measured cross-sections.

At HERA the corrections are larger and more uncertain, as they depend significantly on the assumed shape of the structure functions in the kinematical domain that is so far unexplored.

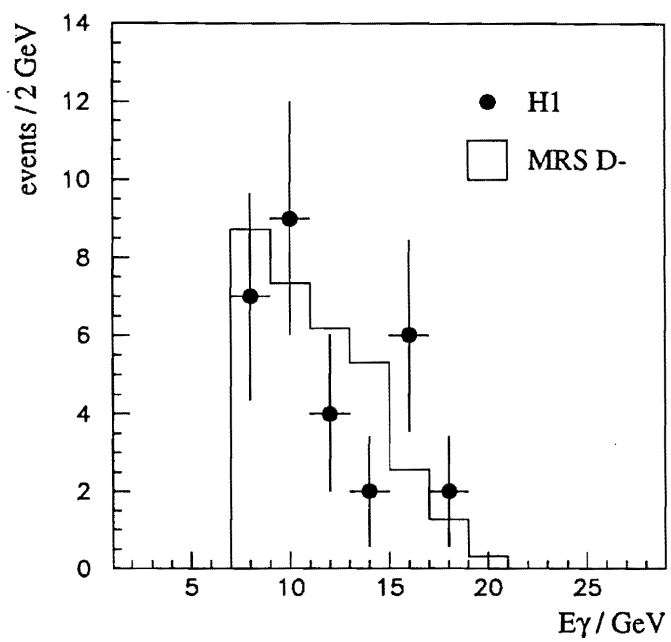

Figure 12: *The spectrum of radiative photons observed in the gamma tagger. The solid line represents the Monte-Carlo predictions obtained with the event generator HERACLES.*

On the other hand, the HERA experiments provide unique possibilities to control and reduce the size of the hard photon radiative corrections [19]. Owing to almost 4π coverage of the hadronic measurement, a large fraction of events containing unobserved hard initial state radiation photons can be identified on the basis of the measured hadronic energy flow. If these events are eliminated, the remaining correction becomes small and, to a large extent, independent of the assumed shape of the structure functions in the unmeasured region.

The radiative corrections are traditionally expressed by $\delta(x, Q^2)$ defined by the equation

$$d\sigma^{meas}/d\sigma^{Born} = (1 + \delta), \tag{8}$$

where σ^{meas} is the measured cross-section for selected events. At low $Q^2 (Q^2 << M_Z^2)$, the dominant contributions to the radiative corrections are coming from purelly electromagnetic processes.

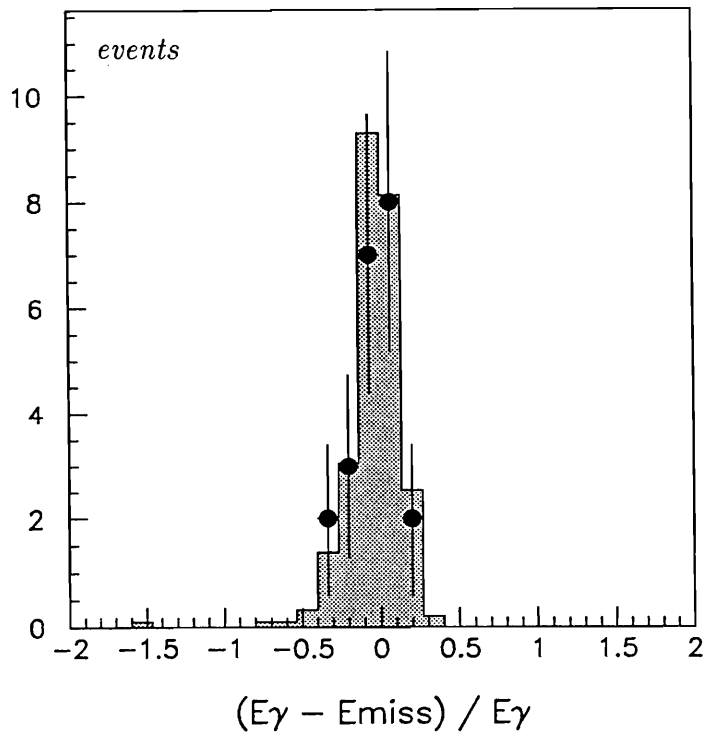

Figure 13: *Cross-check of the reconstruction quality of E_{miss} using events with radiative photons in the photon tagger. E_γ is the radiative photon energy measured in the photon tagger. The shaded histogram represents the Monte - Carlo simulation using the HERACLES program.*

In the fixed target experiments the radiative corrections have been calculated in a fully inclusive way, i.e., integrating over kinematical variables describing emitted real photons. Similar procedure was applied for corrections to the cross section measured in terms of the mixed variables $\delta^m(x, Q^2)$. These corrections were calculated using the TERAD91 program [20] and were found to be lower than 8 % in the measured kinematical domain .

If a similar procedure is applied to calculate the radiative corrections to the cross-section measured in terms of the electron variables, $\delta^e(x, Q^2)$, it turns out that the corrections are large and sensitive to the assumed shape of the parton distribution functions in an unexplored kinematical domain [21]. The corrections are dominated by processes of hard photon emission in a direction close to that of the incident electron. In the H1 detector at HERA a fraction of these photons is observed in the photon tagger, providing an important check of theoretical calculation of the corresponding radiative corrections. In Fig. 12 the observed number of radiative photons with $E_\gamma > 7$ GeV is compared with the prediction of the HERACLES [21] program normalised to the integrated luminosity of the selected event sample. Good agreement is observed both in shape and magnitude. Due to the small angular coverage of the photon tagger most of radiative photons can not be identified in such a direct way. They can, nevertheless, be identified indirectly by measuring a large missing longitudinal energy E_{miss} which can be attributed to a photon emitted in the direction of the incoming electron.

The precision of the E_{miss} reconstruction for radiative events was verified using events in which radiative photons are detected in the photon tagger. For these events one expects $< E_{miss} - E_\gamma >= 0$. For the 1992 data, due to low statistics of the tagged radiative event

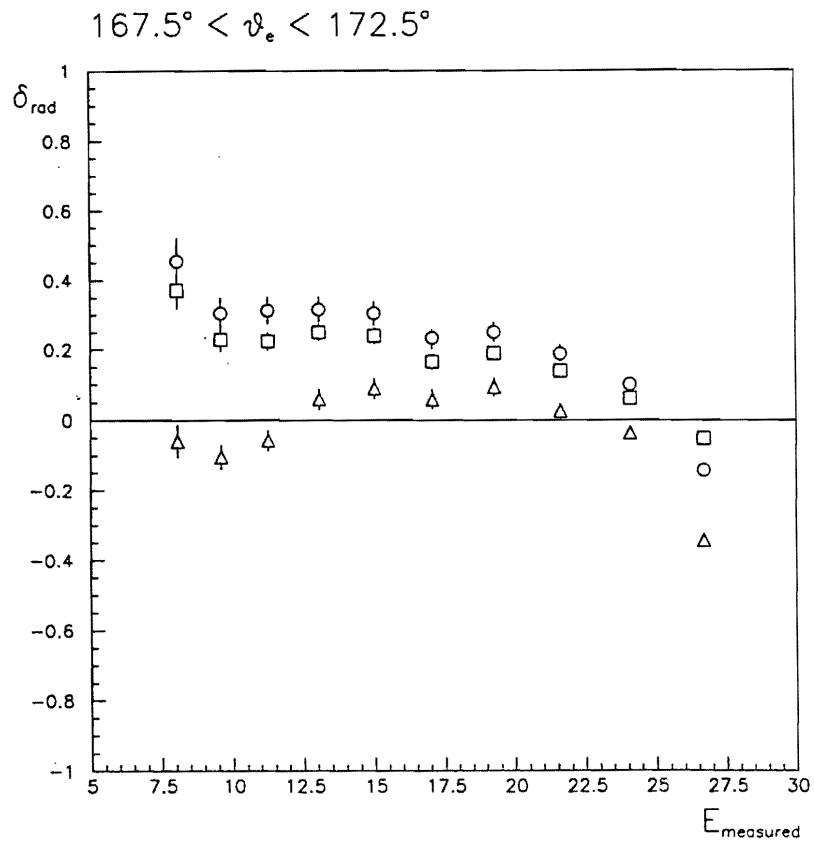

Figure 14: *Reduction of the radiative correction size. Open circles represent the correction calculated in a fully inclusive way, open squares represent corrections calculated for the calorimetric measurement of the scattered electron energy and open triangles represent the correction after applying the E_{miss} cut.*

sample, this equality can been verified with a 5 % accuracy for $E_\gamma > 8GeV$ as shown in Fig. 13. Having established the equality above, it is evident that the E_{miss} cut introduced in section 5.3 rejected effectivly the initial state radiation events of $E_\gamma > 11.7GeV$. The low hadronic mass Compton events [22] were also rejected by demanding a sufficient hadronic activity in the H1 detector such that the interaction vertex is reconstructed. Further reduction of $\delta^e(x, Q^2)$ is obtained owing to a calorimetric measurement of the scattered electron energy as well as a loose cut on the distance between the reconstructed hit in the backward proportional chamber associated with the scattered electron and the corresponding electromagnetic cluster centre of gravity, sensitive to a presence of radiative photons.

The radiative corrections for the sample of events surviving the above rejection criteria have been calculated using the event generator HERACLES [21] and its interface to the fragmentation programs DJANGO [23]. The generated radiative events have been simulated and reconstructed. Applying the defined above, cuts the resulting radiative corrections became small ($\leq$ 10 %) and almost insensitive to the assumed form of the parton distributions, as illustrated in Fig. 14 and 15.

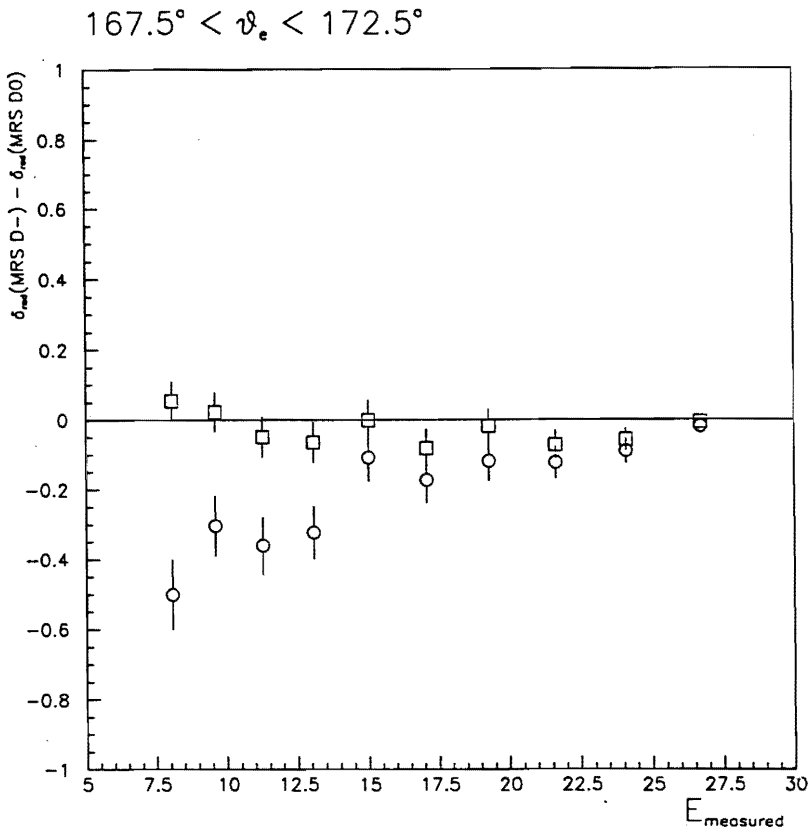

Figure 15: *Sensitivity of the radiative correction size to the assumed form of parton distributions: open circles represent the difference in the radiative correction factor δ calculated in a fully inclusive way for two parametrizations of parton densities (see section 6 for discussion of parton density parametrizations); open squares represent the difference in δ for effective radiative corrections applied for the selected event sample.*

The contribution of the processes of multiple photon emission to the radiative corrections has been estimated using the LESKO program [24]. This contribution has been found to be smaller than 2 % in the measured kinematical domain.

6 Measurement of the proton structure function

6.1 Introduction

Assuming current conservation and invariance under time reversal the cross-section for deep inelastic scattering from an unpolarised target nucleon can be expressed in terms of three structure functions F_1, F_2 and F_3. For the charged lepton scattering mediated by the virtual photon, only two structure functions F_1 and F_2 are necessary owing to the pure vector current type of electromagnetic interactions. Neglecting the lepton masses

and weak interaction effects, the cross-section can be written as:

$$\frac{d\sigma^{ep}}{dxdy} = \frac{4\pi\alpha^2 s}{Q^4}(y^2 x F_1^{ep}(x,Q^2) + (1-y)F_2^{ep}(x,Q^2)), \tag{9}$$

where α is the electromagnetic coupling constant. Another decomposition of the differential cross-section can be made in terms of photoabsorbtion cross-section for right-handed ($\sigma_+(x,Q^2)$), left-handed ($\sigma_-(x,Q^2)$) and longitudinally ($\sigma_L(x,Q^2)$) polarised vector boson. In case of the electromagnetic interaction $\sigma_+ = \sigma_-$ and photoabsorbtion cross-sections σ_L and $\sigma_T = \frac{1}{2}(\sigma_+ + \sigma_-)$ are related to the structure functions by:

$$F_1^{ep}(x,Q^2) = \frac{JM}{4\pi^2\alpha}\sigma_T^{ep}(x,Q^2)$$

$$F_2^{ep}(x,Q^2) = \frac{J\nu}{4\pi^2\alpha}\left(\frac{Q^2}{Q^2+\nu^2}\right)(\sigma_T^{ep}(x,Q^2) + \sigma_L^{ep}(x,Q^2)), \tag{10}$$

where: $J = (W^2 - M^2)/2M$. Using the equations above, the cross-section ratio of longitudinally and transverse polarised photons $R = \sigma_L/\sigma_T$ can be written in terms of structure functions as:

$$R = \frac{F_2}{2xF_1}\left(1 + \frac{Q^2}{\nu^2}\right) - 1 = \frac{F_L}{2xF_1}. \tag{11}$$

At HERA, the structure functions can be measured for the first time for the values of x in the range $x = 10^{-2} - 10^{-4}$ in the deep inelastic regime ($Q^2 > 5$ GeV^2). At present the ratio $R(x,Q^2)$ remains unmeasured in this region. Therefore, in order to extract $F_2(x,Q^2)$ from the measured differential cross-section, the R shape had to be assumed. The R values were calculated according to the QCD prescription [25] using the MRSD−parton distributions [29]. The assumed form of R_{QCD} gives rise to an increase of the cross-section by at most 7 % with respect to the $R = 0$ assumption.

The measurement of F_2 is important for many reasons. The x shape and Q^2 dependence of F_2 in this x range cannot be reliably predicted by extrapolating present fixed target data. Available parametrizations for the low x region rely on model assumptions which have to be confronted with experimental results. If, as was discussed in section 4, $F_2(x,Q^2)$ grows sufficiently fast at low x, HERA will allow us to test perturbative QCD in the domain of high parton densities where both the GLAP and BFKL equations may fail. The measurement of F_2 at low x is indispensible for the interpretation of hard collisions at future hadron colliders both for pp and heavy ion collisions in the quark-parton picture.

6.2 Acceptance and efficiency studies

The differential cross-section was, determined by the H1 collaboration, using several separate analysis methods of the "low Q^2" data sample. Different combinations of kinematical variables and different unfolding procedures were applied.

Two of these methods are discussed in this chapter.

In method I, the event kinematics was calculated from the scattered electron variables. The acceptance, efficiency and cross-section were determined in $\sqrt{E'_e}, \theta_e$ bins which match the resolution and geometrical acceptance of the detector. The calculated cross-sections

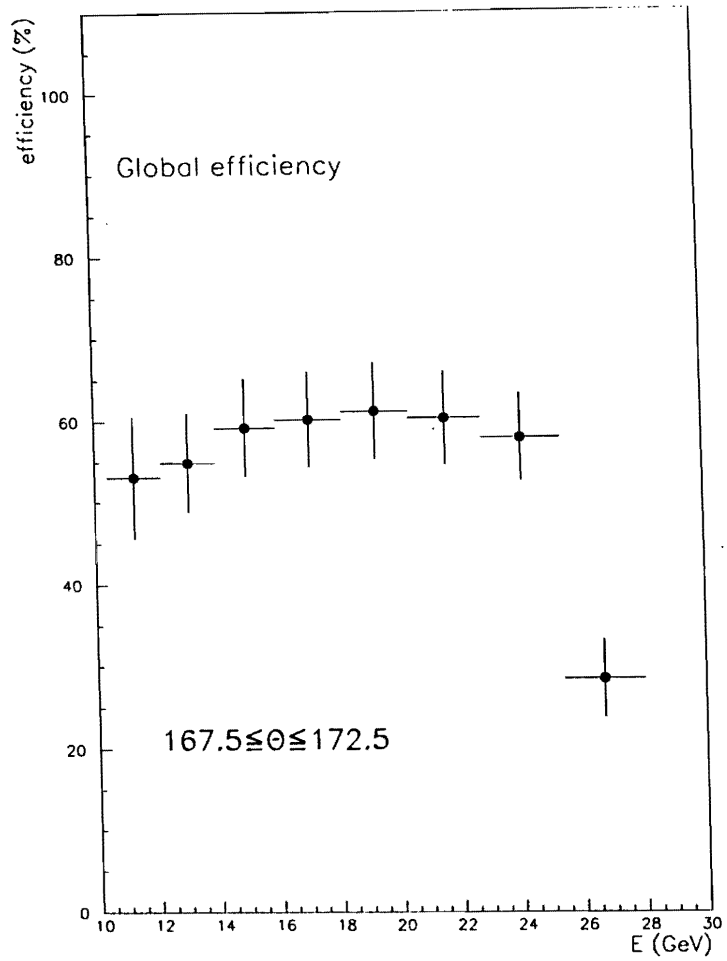

Figure 16: *The efficiency of the event selection for the largest θ_e bin, as a function of the scattered electron energy. The systematic and statistical errors are added in quadrature.*

in these detector oriented bins were then transformed to cross-sections in x_e and Q_e^2. In method II, bins in the variables x_m, eq. (5), and Q_e^2 were used directly for cross-section, acceptance and efficiency calculations.

In method I three equidistant θ_e bins and eight equidistant bins in $\sqrt{E'_e}$, matching the energy dependence of the BEMC resolution, were used. In method II three Q^2 bins and four x bins per decade were chosen. The choice of large bin sizes in both methods is determined by the limited statistics of the data rather than by resolution considerations. As a result smearing corrections are less than 10% everywhere.

The redundancy of the H1 apparatus allows to determine all efficiencies of the cuts used to select the final data sample directly from the data. The overall efficiency of event selection is shown in Fig. 16 for the largest θ_e bin of the method I. The uncertainty of the event selection efficiency is dominated by uncertainties in the measured "electron signatures" as well as by uncertainties in the efficiency of vertex reconstruction, which is low at the highest energy (in the large x region).

Geometrical acceptance and smearing corrections were determined from detailed simulation of large event samples (they are shown in Fig. 17 for the largest θ_e bin of the method I). These corrections were found to be almost independent of the form of input

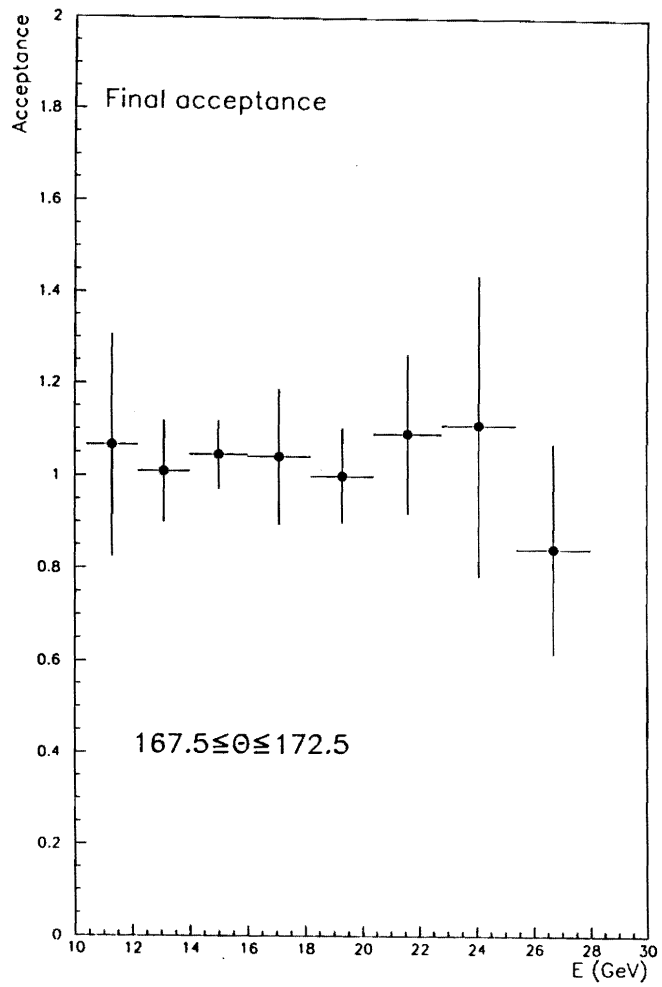

Figure 17: *The smearing and geometrical acceptance correction factors for the largest θ_e bin, as a function of the scattered electron energy. The errors represent the systematic uncertainty of the correction factors due to effects discussed in section 6.3.*

parton densities. The measured differential cross-sections are extrapolated to the centre of each bin using the MRSD− parametrization of parton densities. The corrections are below 10 % and do not depend significantly on the exact shape of F_2.

6.3 The structure function $F_2(x, Q^2)$

The H1 collaboration measured $F_2(x, Q^2)$ in four different Q^2 bins, with the central values of 8.5, 15, 30 and 60 GeV^2. The results of these measurements have been presented in [11]. In the lowest Q^2 bin only the low x region is accessible due to the limited angular acceptance of the BEMC. In this region the F_2 measurement of method I is systematically superior to method II relying on the hadronic measurement of y. In the highest Q^2 bin , the high x domain is accessed, where the results based on the mixed (x_m, Q_e^2) variables (method II) are more accurate than the electron measurement. For the two intermediate Q^2 values both methods yield similar precision and a meaningful comparison can be made.

The F_2 measurements of method I and II is shown in Fig. 18 for two Q^2 values, together with data points from the NMC [26] and BCDMS [27] fixed target muon proton

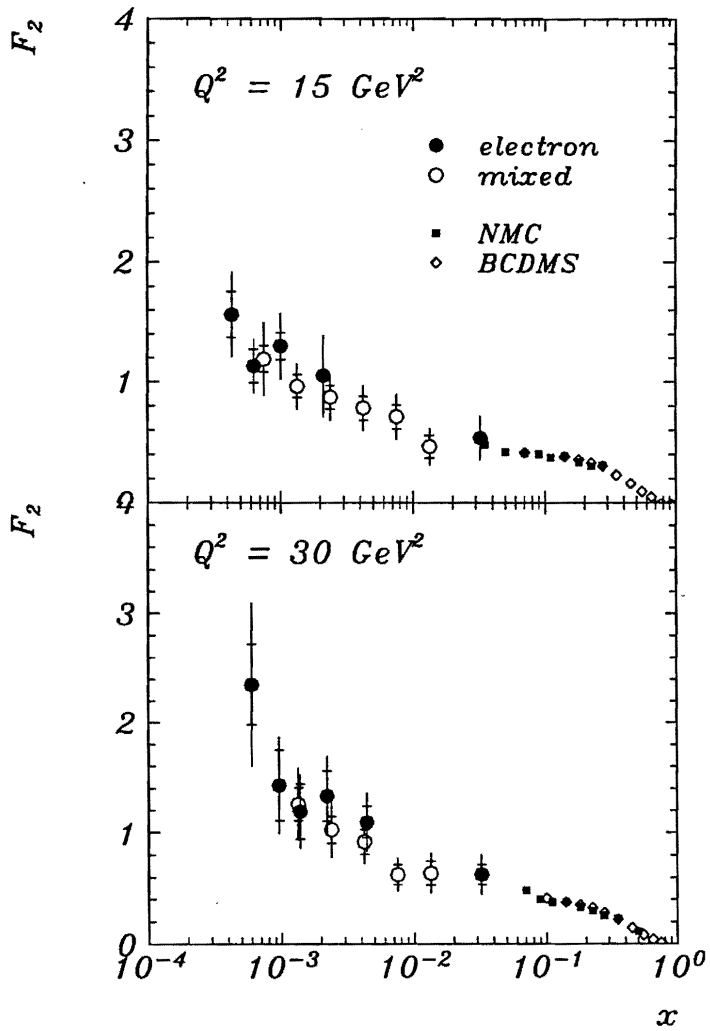

Figure 18: *The $F_2(x, Q^2)$ values as a function of x for two Q^2 bins. The full circles correspond to method I and the open circles to method II. The error bars show statistical and total errors obtained by adding statistical and systematic errors in quadrature. Data points of the NMC and BCDMS experiments are shown for comparison.*

scattering experiments. The statistical and point dependent systematic errors are added in quadrature. The systematic point-to-point error includes: possible shifts of the electron energy scale by 2%; uncertainty in the BEMC energy resolution of 2%; uncertainty in the measurement of y_h including model dependence, an absolute scale uncertainty of the hadronic energy measurement in the LAr calorimeter of 7 %, and effects resulting from the treatment of noise in the calorimeter; possible shifts of θ_e by 5 *mrad*; uncertainty in the event selection efficiency (shown in Fig. 16); uncertainty in the electron and proton beam induced background; uncertainty in the photoproduction contamination; uncertainty in the detector acceptance calculation due to the assumed form of the input parton distributions; uncertainty in the size of the radiative corrections; uncertainty in the bin centre correction. The global systematic error of 8% resulting mostly from the uncertainty of luminosity monitoring is not shown in the figure. The results of method I and of method II, which are to a large extent subject to different systematic effects,

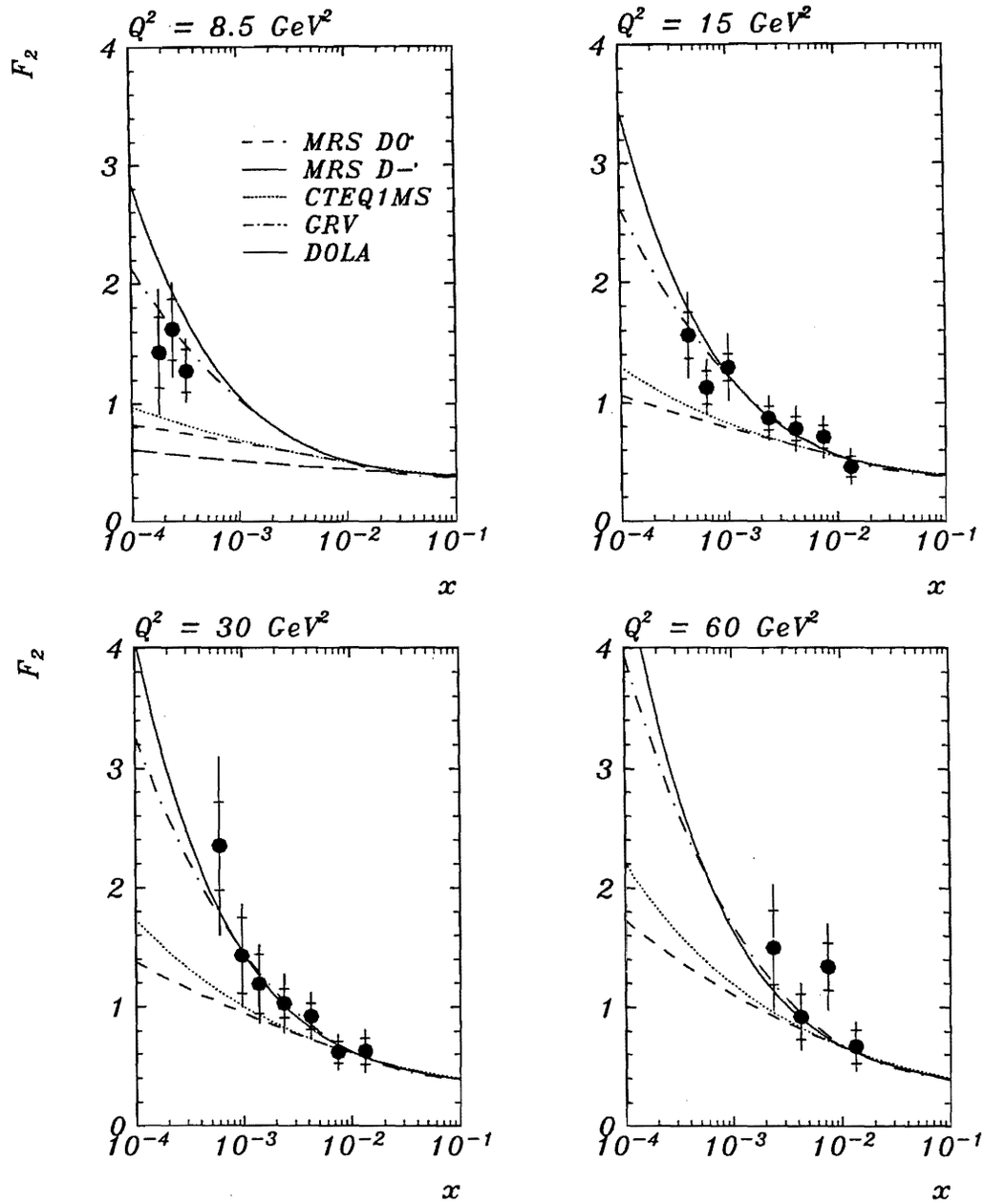

Figure 19: *Comparison of the measured structure function $F_2(x, Q^2)$ with several parametrizations (see text for further explanation). The error bars show statistical and total errors. The overall normalization uncertainty of the data points of 8 % is not included in the size of error bars.*

are found to be in good agreement. The two highest x data points agree well with the available measurements from fixed target experiments yielding an independent cross-check of the absolute normalization with an accuracy of $\sim$ 20%.

A final F_2 in the full range of x and Q^2 is obtained by taking the systematically more accurate F_2 values. The x dependence of F_2 is shown in Fig. 19. A clear rise of F_2 with

decreasing x is observed. The rise of F_2 at small x indicates that high parton density effects may become detectable at HERA. Such a rise is not expected from Regge-parton models [28], but can be accommodated in the models based on the linear QCD evolution equations. Various QCD based models of parton density parametrizations exist. They result from fits to the low energy deep inelastic scattering data. Due to the absence of experimental data prior to the HERA results, these parametrizations generally make assumptions on the behaviour of the parton densities at x values below 10^{-2}. Some examples of F_2 structure functions calculated for different parton density parametrizations are shown in Fig. 19. They include: the MRSD[29] parametrizations where, at small x, the gluon density is either singular (Lipatov behaviour) $\sim x^{-0.5}$ for MRSD$-'$ or constant for MRSD0$'$; the CTEQ1MS[30] parametrization where the gluon density at low x is $\sim x^{-0.5}$, but the sea quark distribution is not strongly coupled to the gluon density, leading to a much slower rise of F_2 with decreasing x; the GRV [31] parametrization, where small x partons are radiativelly generated according to the Altarelli-Parisi equations, starting from "valence-like" quark and gluon distributions at $Q_0^2 = 0.3\ GeV^2$; the DOLA [28] parametrization derived within a Regge phenomenology. These parametrizations describe well the existing low energy fixed target data. They predict, however, the F_2 values at $x \simeq 10^{-4}$ which differ by more than a factor 4. The present measurement favors clearly the MRSD$-'$ and the GRV parametrizations.

7 Study of hadronic system produced in the deep inelastic electron proton scattering

At HERA, owing to a large centre of mass energy the hadronic final state associated with deep inelastic scattering should reflect closelly the parton dynamics. The hadronization effects which dominate at low energies play a less significant role in interpretation of the measurements allowing quantitative tests of Quantum Chromodynamics in this domain.

In the selected data sample, most of the events populate the Q^2 range accessed already in the previous experiments. However, at HERA, this Q^2 domain corresponds to a large hadronic invariant mass W of the hadronic final state (of about 100 GeV) as the average x values of observed events is small. This is clearly a new domain that has not been explored so far. In this section results obtained by the H1 collaboration on the hadronic energy flow and jet production in the deep inelastic scattering events are discussed.

A first measurement of the hadronic final state in the H1 experiment based on a data sample corresponding to an integrated luminosity of $1.6nb^{-1}$ was reported in [32]. The first results on jet production were reported in [33].

7.1 QCD Models and Simulation

In order to interpret the observed distributions in terms of partonic processes, Monte Carlo models are used which include: the parton dynamics controlled by QCD, soft hadronization processes and simulation of the response of the detector. Various prescriptions for the simulation of QCD effects in deep inelastic scattering are compared to the data:

- Leading log parton showers (PS).
  The leading log parton shower models used are those implemented in LEPTO 5.2 [34], labelled PS, and in HERWIG 5.5 [35], labelled HERWIG. In the parton shower approach implemented in LEPTO, the amount of hardness of the gluon radiation depends on the virtuality of the parton before and after the quark-photon vertex. In ep scattering two virtuality scales Q^2 or W^2 are present and each combination of them is allowed by the lower energy experiments. In the H1 experiment one can investigate for the first time the kinematic region where $< Q^2 > \approx 15\ GeV^2$ and $< W^2 > \approx 10^4\ GeV^2$, in which significantly more gluon radiation is predicted using the higher W^2 scale. For comparison with data, three scales Q^2, W^2 and an intermediate scale WQ were chosen. Distributions for each of these cases are denoted with PS(Q^2), PS(W^2) and PS(WQ). In the model implemented in the HERWIG event generator the only energy scale which enters is Q^2. This model contains the colour coherence effects.

- Matrix elements with matched parton showers (ME+PS).
  In this approach, implemented in LEPTO 6.1, the photon gluon fusion and gluon radiation processes are simulated using exact order α_s matrix elements. Soft gluon emission is added using the parton shower model.

- The colour dipole model (CDM).
  This model in contrast to the previous ones does not distinguish between initial and final state radiation. Here the gluon radiation is orginating from colour dipoles initiated by a dipole formed between the scattered quark and the proton remnant. This model is implemented in ARIADNE 4.03 program [36].

7.2 Energy flow

The distributions presented in this section are not corrected for detector acceptance and resolution. The data are compared with model calculations including full simulation of the H1 detector. The detector effects are, however, small (never exceeding 20 %).

The flow of energy measured in the calorimeter transverse to the beam axis, E_T, is shown in Fig.20a, for "low Q^2" events, as a function of pseudorapidity $\eta = -\ln\tan\frac{\theta}{2}$. Here θ is the polar angle of the energy deposition. Fig.20b shows the flow of E_T, measured with the calorimeter in the rapidity interval $-3 < \eta < 3$, as a function of ϕ. Here ϕ is the angle in the plane transverse to the beam direction between the scattered electron and the energy deposition. One observes the current jet as a collimated energy flow balancing the p_T of the electron at $\phi = \pi$. The ME+PS and the CDM models are in good agreement with the data. The parton shower simulation PS(W^2), predicts too large transverse energy, whereas PS(Q^2) predicts to small transverse energy flow. It has to be stressed that no attempt has been made to tune the parameters of the above models.

In Fig. 21 the x_F ($x_F = 2p_z^*/W$) dependence of the mean transverse momentum squared measured in the centre of mass reference system is shown. In this frame the z^* axis is defined as the direction of the exchanged virtual photon. In the naive quark parton model the current and target jet fragmentation regions then correspond to the $+z^*$ and $-z^*$ hemispheres. In the hadronic CMS the distribution of particle momenta transverse to the virtual photon direction as a function of x_F is particularly sensitive to different QCD models. The PS(WQ), HERWIG and the ME+PS model describe the data quite

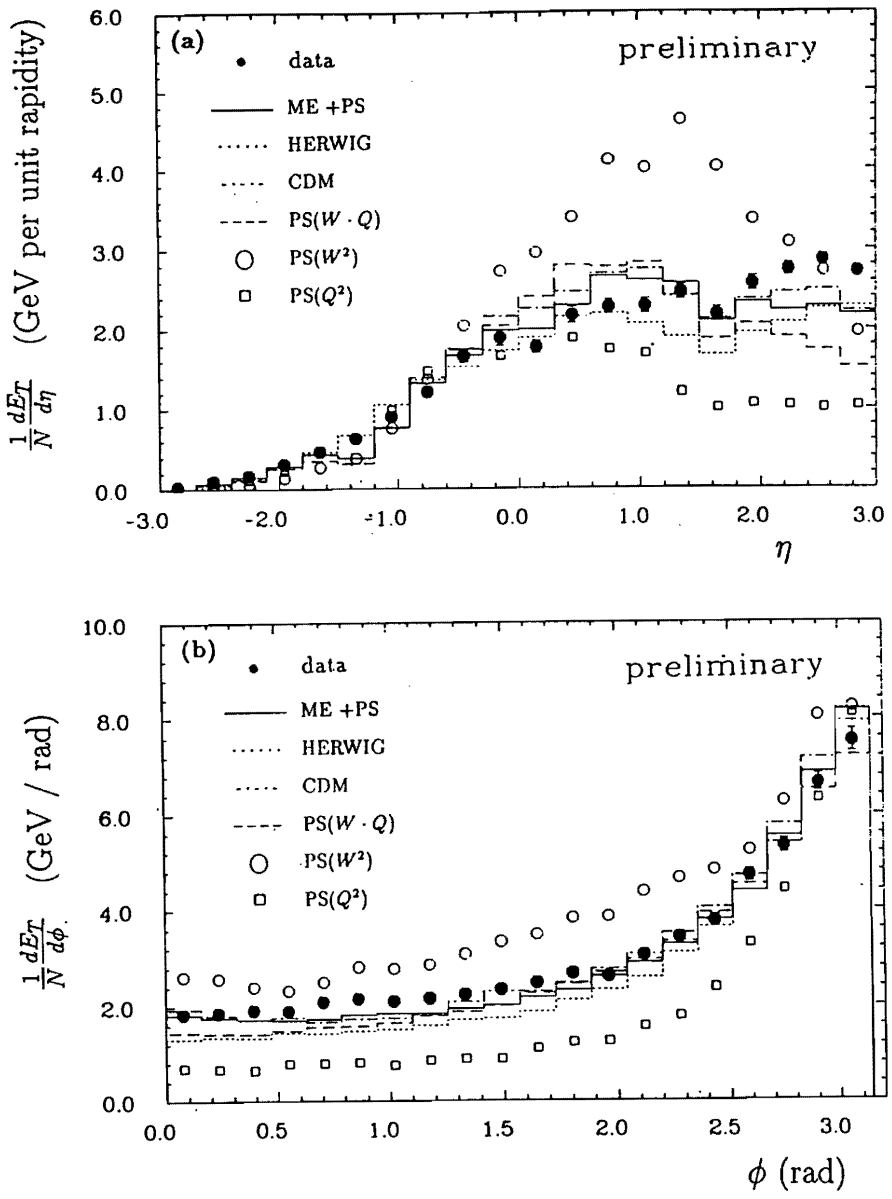

Figure 20: *Transverse energy flow E_T as a function of pseudorapidity η (a) and as a function of azimuthal angle ϕ (b) with respect to the scattered electron direction in the plane transverse to the beam directions. The predictions of models discussed in the text are also given.*

well. The CDM model underestimates the average transverse momenta in the whole x_F range.

7.3 Jet Rates

In the analysis of the jet production the JADE algorithm [37] was used and performed in the laboratory frame. Several Lorenz frames and other jet algorithms were investigated.

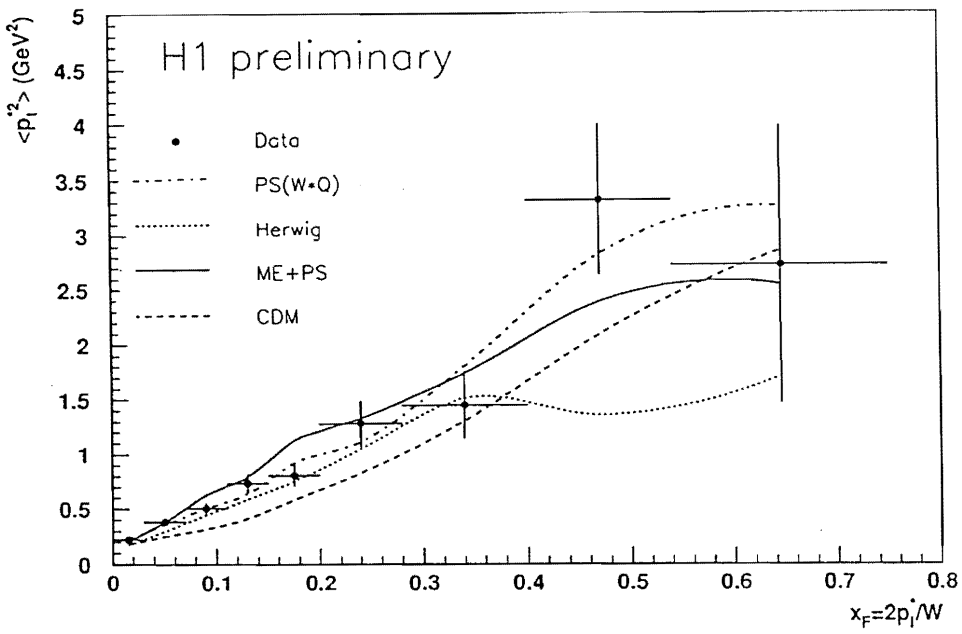

Figure 21: *Average p_T^{*2} as a function of x_F. Comparison of the data and the model predictions.*

No significantly better agreement of the jet rates at the parton level with those obtained at the hadron level was achieved.

In the JADE algorithm the "particle" 4-vectors are reconstructed using the calorimeter cell energies and the vector joining the reconstructed event vertex with the centre of the cells. The invariant mass of all "particle" pairs (or combined objects) (i, j) is calculated using $m_{ij}^2 = 2E_iE_j(1 - cos\theta_{ij})$, thus neglecting the masses of "particles" i and j. The pair with the smallest mass is taken to form a new combined object k by adding the 4-vectors, $p_k = p_i + p_j$. The procedure is repeated until all remaining pairs have masses m_{ij} exceeding a cut-off which is defined by $m_{ij}^2 > y_{cut}M^2$, where y_{cut} is a resolution parameter and M is a mass scale taken to be the invariant mass of all objects entering the cluster algorithm. The energy deposition attributed to the scattered electron is excluded from this procedure. To account for the loss in the beam pipe of most hadrons from the proton, a remnant pseudoparticle was introduced with its longitudinal momentum given by the missing longitudinal momentum of the event and no transverse momentum.

The dependence of the jet rates on the resolution parameter y_{cut} is shown for the low and high Q^2 data sample in Fig.22 a and b respectively.

The data are not corrected for detector bias. R_{N+1} is the fraction of $(N+1)$ jet events in the sample (the 1+1 configuration corresponds to a current and a target remnant jet). At $y_{cut} = 0.02$, the (1+1) and (2+1) classes dominate, with $R_{2+1} \approx 10$ to 20%. It should be noted that the data points in Fig.22 are strongly correlated as the same event sample is used for each value of y_{cut}. In Fig. 22 only the statistical errors are given.

To check if these rates reflect jet multiplicities at the parton level, the data are compared to Monte Carlo predictions at the parton level (dotted curve), to the same model after hadronization (dashed curve), and to the prediction including a complete simulation of the H1 detector (full curve). In all cases the ME+PS model is used. The figure

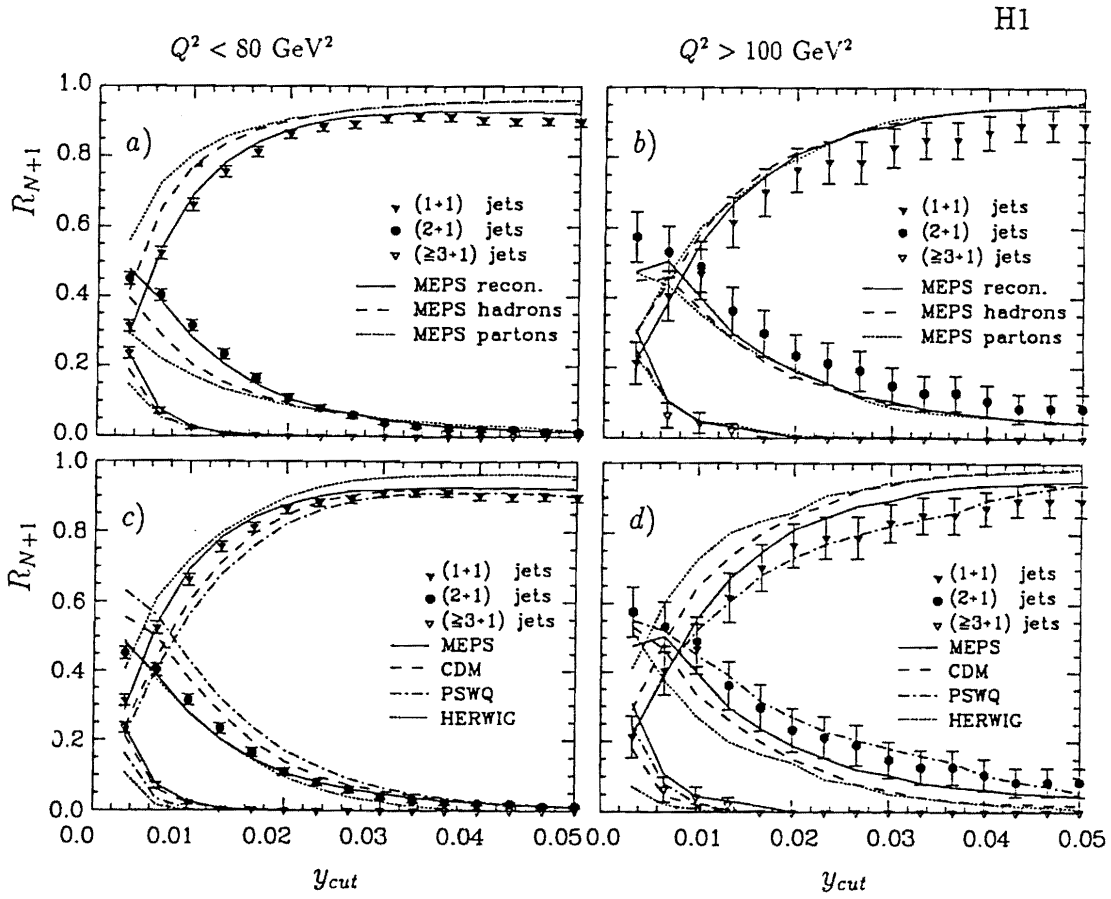

Figure 22: *Fractions of N+1 jets as a function of y_{cut} for the "low Q^2" (a,c) and for the "high Q^2" (b,d) sample compared with simulations using MEPS model (a,b) and other models (c,d) discussed in the text. and the model predictions.*

shows clearly that in the high Q^2 sample, hadronization and detector effects are small ($\approx 10\%$). For the low Q^2 sample, the differences between these curves are larger ($\approx 15\%$) for $y_{cut} \geq 0.02$. For lower values of y_{cut} more "jets" are resolved because the jet algorithm often fails to include individual hadrons in jet clusters.

It should be noted that there exists migrations of events classified as (2+1) jet at the parton level to the (1+1) class at the hadron level and vice versa. This migration is due to the finite resolution of the y_{cut} value at which a (2+1) jet event is turned into a (1+1) event at the parton and hadron levels. .

All QCD-based models discussed in section 7.1 reproduce the dependence of the jet rates upon y_{cut} for both "low Q^2" and "high Q^2" data samples, as shown in Fig. 22. The PSWQ model prediction of the (2+1) jet rate in the region around $y_{cut} = 0.02$ shows the most significant deviation from the data, namely by $\approx +50\%$ at $Q^2 < 80$ GeV^2.

The Q^2 dependence of R_{2+1} is shown in Fig. 23 for fixed $y_{cut} = 0.02$ together with the expectation of the different models discussed above. The experimental points are well described by the MEPS model. The PSWQ model results systematically exceed the measurement. R_{2+1} using HERWIG and especially CDM shows little Q^2 dependence.

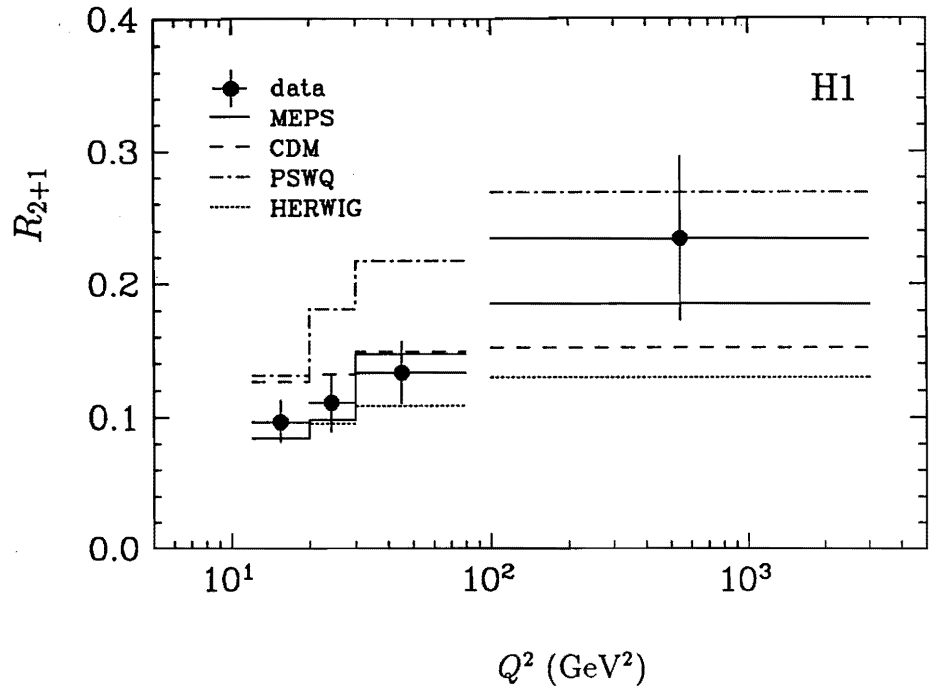

Figure 23: *(2+1) jet fraction corresponding to* $y_{cut} = 0.02$ *as a function of* Q^2 *compared with different model (see text) predictions.*

8 Search for leptoquarks

The *ep* collider HERA is well suited to look for leptoquarks. If exist, they will be produced as *s*-channel resonances between the incoming electron and a constituent of the proton.

Leptoquark bosons appear naturally, and possibly at accessible masses, in some grand unified theories [38], in superstring inspired models [39], in technicolour [40] and in some composite models [41].

In the narrow width approximation, the production cross-sections for leptoquarks can be described by a simple formula:

$$\sigma_{ep} \propto (\Gamma f(x)/M) \tag{12}$$

where M is the mass of the heavy state and $f(x)$ describes the quark density in the proton. The widths Γ contain the model dependence on the couplings of the new particles and can be expressed as $\Gamma = (\lambda^2/16\pi)M$ for scalar and $\Gamma = (\lambda^2/24\pi)M$ for vector leptoquarks.

The results presented in this section have been reported in [42].

In Table 3 the isospin multiplets of scalar and vector leptoquarks characterised by their electric charge are listed. They represent the first generation of baryon and lepton number conserving scalar and vector bosons having $SU(3) \otimes SU(2) \otimes U(1)$ invariant couplings to fermions. The effective Lagrangian for their interactions has been introduced in [43].

For leptoquark searches in the $e + X$ final states, the "high $Q2$" event sample was used. In addition to selection criteria specified in section 5 a matching between y_e and y_h was required: $\mid y_e - y_h \mid < 0.3$ corresponding to a more stringent E_{miss} cut than the one

F=2	T_3	prod. decay	$\mathcal{B}$	F=0	T_3	prod. decay	$\mathcal{B}$
${}^{-1/3}S_0$	0	$e_L^- \, u_L \to e^- \, u$	1/2	${}^{-2/3}V_0$	0	$e_L^- \, \bar{d}_R \to e^- \, \bar{d}$	1/2
		$\to \nu_e \, d$	1/2			$\to \nu_e \, \bar{u}$	1/2
		$e_R^- \, u_R \to e^- \, u$	1			$e_R^- \, \bar{d}_L \to e^- \, \bar{d}$	1
${}^{-4/3}\tilde{S}_0$	0	$e_R^- \, d_R \to e^- \, d$	1	${}^{-5/3}\tilde{V}_0$	0	$e_R^- \, \bar{u}_L \to e^- \, \bar{u}$	1
${}^{-4/3}S_1$	-1	$e_L^- \, d_L \to e^- \, d$	1	${}^{-5/3}V_1$	-1	$e_L^- \, \bar{u}_R \to e^- \, \bar{u}$	1
${}^{-1/3}S_1$	0	$e_L^- \, u_L \to e^- \, u$	1/2	${}^{-2/3}V_1$	0	$e_L^- \, \bar{d}_R \to e^- \, \bar{d}$	1/2
		$\to \nu_e \, d$	1/2			$\to \nu_e \, \bar{u}$	1/2
${}^{+2/3}S_1$	1	None		${}^{+1/3}V_1$	1	None	
${}^{-4/3}V_{1/2}$	$-1/2$	$e_R^- \, d_L \to e^- \, d$	1	${}^{-5/3}S_{1/2}$	$-1/2$	$e_L^- \, \bar{u}_L \to e^- \, \bar{u}$	1
		$e_L^- \, d_R \to e^- \, d$	1			$e_R^- \, \bar{u}_R \to e^- \, \bar{u}$	1
${}^{-1/3}V_{1/2}$	$+1/2$	$e_R^- \, u_L \to e^- \, u$	1	${}^{-2/3}S_{1/2}$	$+1/2$	$e_R^- \, \bar{d}_R \to e^- \, \bar{d}$	1
${}^{-1/3}\tilde{V}_{1/2}$	$-1/2$	$e_L^- \, u_R \to e^- \, u$	1	${}^{-2/3}\tilde{S}_{1/2}$	$-1/2$	$e_L^- \, \bar{d}_L \to e^- \, \bar{d}$	1
${}^{+2/3}\tilde{V}_{1/2}$	$+1/2$	None		${}^{+1/3}\tilde{S}_{1/2}$	$+1/2$	None	

Table 3: *Isospin multiplets T of scalar ${}^{Q}S_T$ and vector ${}^{Q}V_T$ leptoquarks with electric chage Q, branching ratio B and fermion number F.*

used in the structure function analysis. For leptoquark searches in the $\nu + X$ final states, a missing transverse momentum of $P_T^{miss} \equiv \sqrt{(\sum E_x)^2 + (\sum E_y)^2} > 20$ GeV measured by the calorimeters was required. Events with an electron candidate with $E_T^e > 10$ GeV were rejected.

A leptoquark clearly would be seen as a resonance in a mass plot. Leptoquarks would show up on top of the DIS background as a narrow resonance centred at a mass $M \simeq \sqrt{x\,s}$. For an $e + X$ event, the resonance mass is calculated using $M = \sqrt{s x_e}$. For a $\nu + X$ event candidate, the mass is calculated as $M = \sqrt{s x_h}$ where x_h is computed from the measured hadronic energy flow as:

$$x_h = (P_{T,h}^2)/((1 - y_h)\, y_h s) \tag{13}$$

The selected data sample was compared to Monte Carlo expectations based on the DJANGO event generator [23] which includes first order QED radiative corrections and QCD corrections (leading log parton showers). Fig. 24a shows the measured P_T^{miss} for the 43 $e + X$ measured events compared to the DIS event simulation. The events are well balanced in the transverse plane and the DIS Monte Carlo reproduces well the tail of the P_T^{miss} distribution which is due to detector resolution and energy losses. The mass distribution is shown in Fig. 24b before and after a final kinematical cut of $y_e > 0.25$. This cut was chosen as a compromise to optimise the signal-to-background ratio for scalar leptoquark searches while maintaining efficient detection of vector leptoquarks. It also safely rejects the low y region where both y_e and x_e are badly measured. In Fig. 24b, both the absolute number of events and the shape of the mass spectra are well reproduced by a DIS Monte Carlo simulation before and after the y_e cut. For the $\nu + X$ final states, no additional kinematical cuts are applied and a mean number of 0.66 charged current events are predicted by the Monte Carlo simulation after folding in the LAr trigger efficiencies

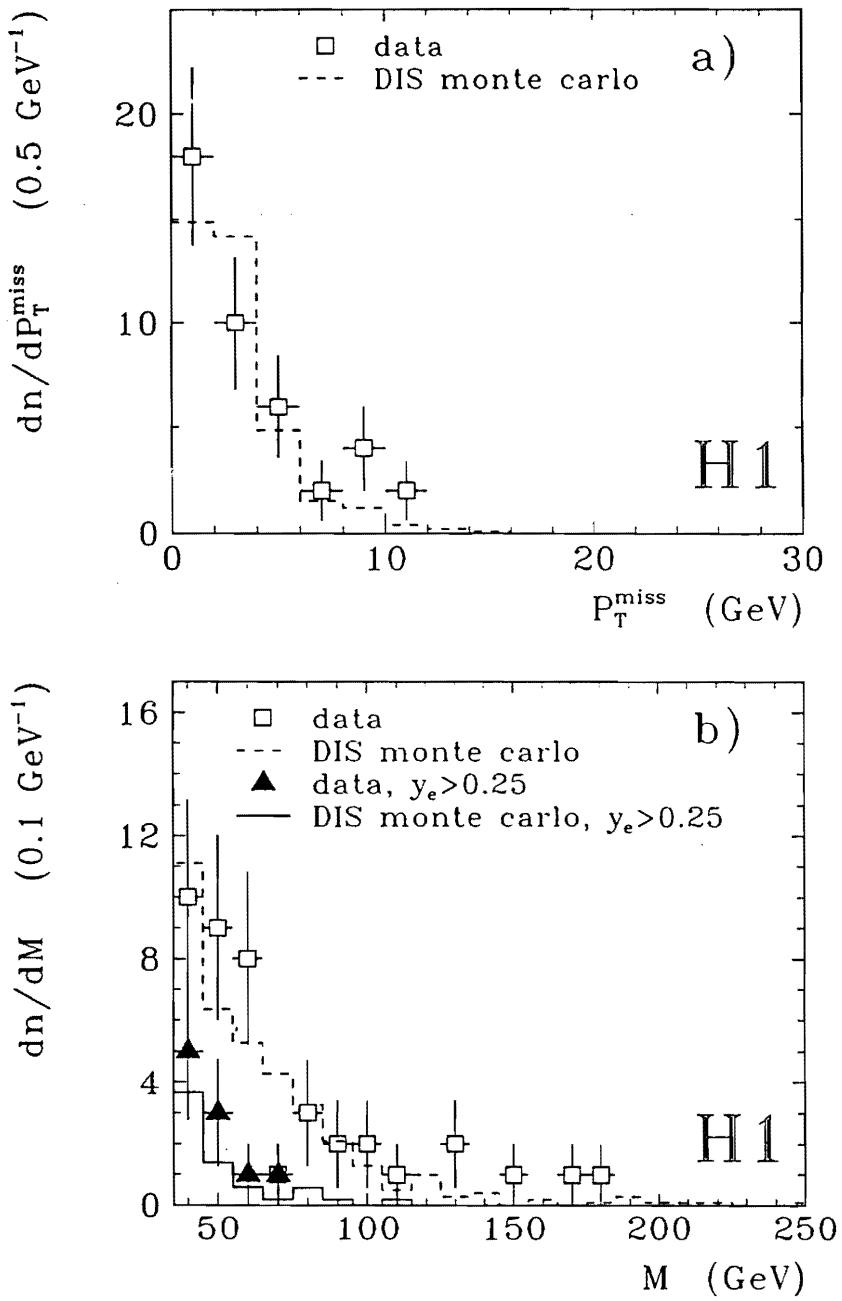

Figure 24: *The P_T^{miss} distribution (a) and mass spectrum (b) for before (open points) and after (closed points) the cut on y_e. The histogram curves show the absolute prediction of a DIS Monte Carlo simulation before (dashed) and after (solid) the y_e cut.*

for the hadronic flow. The data samples are compatible with expectations from standard DIS background. Consequently, one can derive rejection limits under the hypothesis that all observed events are originate from such background.

The rejection limits on the mass versus coupling constant plane are shown in Fig. 25.

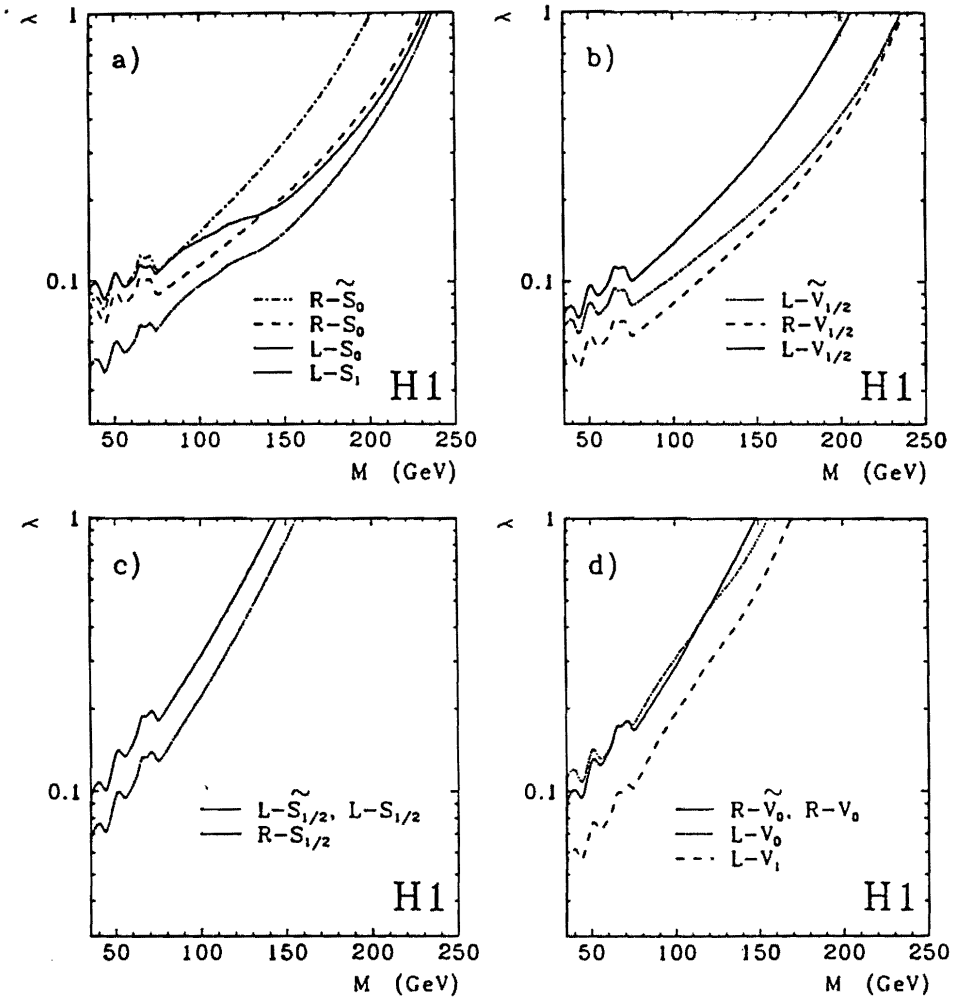

Figure 25: *Rejection limits at the 95% CL for the coupling $\lambda_{L,R}$ as a function of mass for scalar and vector leptoquarks with fermion number F=2 (a), (b) and F=0 (c), (d). The regions above the curves are excluded.*

For $\lambda = 0.3$ coupling, which corresponds to an electromagnetic coupling ($\alpha = \frac{\lambda^2}{4\pi}$), the mass limits at 95% CL are:
$M \geq 181\,(S_0^L)$, $178\,(S_0^R)$, $145\,(S_0^R)$, $192\,(\tilde{S}_0^R)$, $152\,(V_{1/2}^L)$, $190\,(V_{1/2}^R)$ and 183 GeV $(\tilde{V}_{1/2}^L)$ for leptoquarks resulting from electron fusion with quarks and:
$M \geq 98\,(V_0^L)$, $102\,(V_0^R, \tilde{V}_0^R)$, $121\,(V_1^L)$, $98\,(S_{1/2}^L, \tilde{S}_{1/2}^L)$ and 112 GeV $(S_{1/2}^R)$ in the case of fusion with antiquarks. The current limits from $p\bar{p}$ experiments have thus been improved after only a few months of data taking on HERA (for the S_0^L (S_0^R) leptoquarks, which are characterised by a branching ratios of $\mathcal{B} = 50\%\,(100\%)$ for $e + X$ decays, the CDF limits [44] are 82 GeV (113 GeV) almost independently of the coupling λ).

9 Conclusions

The H1 results obtained in the analysis of deep inelastic scattering data corresponding to integrated luminosity of 22.5 nb^{-1} has been presented. The measured F_2 structure

function exhibits a significant rise with decreasing x. Global features of the hadronic system produced in deep inelastic scattering have been compared with model predictions. The parton shower approach fails if either W^2 or Q^2 scale is chosen as a scale of quark virtuality. The MEPS model describe well the characteristics of the hadronic system including the Q^2 dependence of the jet rates. No leptoquarks have so far been found.

Acknowledgements

I am very grateful to all my colleagues of the H1 collaboration for their effort in getting the results presented in these lectures. I thank all my colleagues from the radiative correction group and the Brussels-Paris-Saclay analysis group, in particular to Marc Besançon, François Charles, Andre Courau, Eric Evrard, Laurent Favart, Manfred Fleischer, Marcel Goldberg, Nguyen Khan, Smain Kermische, Jean-François Laporte, Pierre Marage, Uve Obrock, Arkadii Panitch Pal Ribarics, Robert Rosen, Christophe Royon, Patrick VanEsch, for many fruitful discussions and help in preparation of several plots for these lectures. I thank also Joel Feltesse, Alan Percus, Jean-François Laporte and Marcel Goldberg for critical reading of the manuscript.

References

[1] E. D. Bloom et al., Phys.Rev.Lett **23** (1969) 930.

[2] M. Breidenbach et al., Phys.Rev.Lett. **23** (1969) 935.

[3] G. Miller et al., Phys.Rev. **D5** (1972) 528.

[4] J.D. Bjorken, Phys.Rev. **179** (1969) 1547.

[5] J.D. Bjorken, A. Paschos, Phys.Rev. **185** (1969) 1975.

[6] R.P. Feynman, Photon-Hadron Interactions (W.A. Benjamin Co., New York, 1972).

[7] H.Fritzsch, M. Gell-Mann, H. Leutwyler, Phys.Lett. **47B** (1973) 365.

[8] H.D. Politzer, Phys.Rev.Lett. **30** (1973) 1346.

[9] D. Gross, F. Wilczek, Phys.Rev.Lett. **30** (1973) 343.

[10] M. Virchaux, Invited talk at the Workshop "QCD - 20 years later" Aachen, 9-13 June 1992, DAPNIA/SPP 92-30.

[11] H1 Collab., T. Ahmed et al., DESY-93-117, Aug 1993. To be published in Nucl. Phys. B.

[12] J. Gayler, to be published in the Proceedings of the 3rd Int. Conf. on Calorimetry in High Energy Physics, Corpus Christi, 1992.

[13] A.Blondel and F.Jacquet, Proceedings of the Study of an *ep* Facility for Europe, ed. U.Amaldi, *DESY* **79/48** (1979) 391

[14] G. Altarelli, G. Parisi, Nucl. Phys.**B126** (1977) 297

[15] E.A.Kuraev, L.N.Lipatov and V.S.Fadin, Phys.Lett. **60B** (1975) 50; Zh.E.T.F **72** (1977) 377

[16] V.N Gribov, E.M. Levin and M.G. Ryskin, Sov.Journ.Nucl.Phys. **15**, (1972) 438 and 675.

[17] T. Ahmed et al., Phys.Lett. **299B** (1993) 374.

[18] D. Yu. Bardin, C. Burdik, P. Ch. Christova, T. Riemann, Z.Phys **42** (1989) 679. M. Böhm, H. Spiesberger, Nucl. Phys. **B294** (1987) 1081.

[19] M. W. Krasny, Proceedings of the Workshop "Physics at HERA", ed. W. Buchmüller and G. Ingelman, Hamburg, (1991) 850.

[20] A. Akhundov et al., Proceedings of the Workshop "Physics at HERA", ed. W. Buchmüller and G. Ingelman, Hamburg, (1991) 1285.

[21] H.Spiesberger et al. , Proceedings of the Workshop "Physics at HERA", ed. W. Buchmüller and G. Ingelman, Hamburg, (1991) 798.

[22] A. Courau et al. , Proceedings of the Workshop "Physics at HERA", ed. W. Buchmüller and G. Ingelman, Hamburg, (1991) 902.

[23] G.S. Schuler and H. Spiesberger, Proc. of the Workshop Physics at HERA, DESY, Hamburg (October 1991) Vol. 3 p 1419 (DJANGO version 1.0), and references therein.

[24] W. Placzek, Proceedings of the Workshop "Physics at HERA", ed. W. Buchmüller and G. Ingelman, Hamburg, (1991) 1433.

[25] G. Altarelli, G. Martinelli, Phys.Lett. **76B** (1978) 89.

[26] NMC Collab., P. Amaudruz et al., Phys. Lett. **295B** (1992) 159 and Erratum to CERN-PPE/92-124, CERN, April 1993.

[27] BCDMS Collab., A.C. Benvenuti et al., Phys.Lett. **223B** (1989) 485.

[28] A. Donnachie, P. V. Landshoff, M/C-th 93/11, DAMTP 93-23.

[29] A. D. Martin, W. J. Stirling, R. G. Roberts, Phys.Lett. **306B** (1993) 145, ibid. **309B** (1993) 492.

[30] J. Botts et al., Phys. Lett. **304B** 159,1993

[31] M. Glück, E. Reya and A.Vogt, Z.Phys. **C53** 127 (1992); M. Glück, E. Reya and A.Vogt, Phys. Lett. **B306** 391,1993.

[32] H1 Collab., T. Ahmed et al., Phys. Lett. **298B** (1993) 469.

[33] H1 Collab., I. Abt et al., DESY-93-137, Oct. 1993.

[34] G. Ingelman, "LEPTO 5.2", unpublished program manual; H.Bengtsson, G.Ingelman, and T.Sjöstrand, Nucl. Phys. **B301** (1988) 554;

[35] G. Marchesini, B.R. Webber, G. Abbiendi, I.G. Knowles, M.H. Seymor, and L. Stanco, Comp.Phys.Comm. **67** (1992) 465, and references therein.

[36] L. Lönnblad, ARIADNE version 4.03, Comp. Phys. Commun. 71 (1992) 15, and references therein.

[37] JADE Collab., W. Bartel et al. Z. Phys. **C33** (1986) 23

[38] J.C. Pati and A. Salam, Phys. Rev. **D10** (1974) 275; P. Langacker, Phys. Rep. **72** (1981) 185; G. Senjanović and A. Šokorac, Z. Phys. **C20** (1983) 255.

[39] V.D. Angelopoulos et al., Nucl. Phys. **B292** (1987) 59; A. Dobado, M.J. Herrero and C. Muñoz, Phys. Lett. **B191** (1987) 447.

[40] S. Dimopoulos and L. Susskind, Nucl. Phys. **B155** (1979) 237; S. Dimopoulos, Nucl. Phys. **B168** (1980) 69; E. Farhi and L. Susskind, Phys. Rev. **D20** (1979) 3404; Idem, Phys. Rep. 74 (1981) 277.

[41] B. Schrempp and F. Schrempp, Phys. Lett. **B153** (1985) 101, and references therein.

[42] The H1 results on new particle searches were recently discussed in: H1 Collab., Nucl. Phys. **B396** (1993) 3.

[43] W. Buchmüller, R. Rückl and D. Wyler, Phys. Lett. **B191** (1987) 442.

[44] S.M. Moulding, CDF Collab., Fermilab preprint CONF-92-341-E (November 1992).